Sustainable Energy & Fuels

REVIEW

View Article Online
View Journal | View Issue

Cite this: *Sustainable Energy Fuels*, 2018, **2**, 1375

The quest for manganese-rich electrodes for lithium batteries: strategic design and electrochemical behavior

M. M. Thackeray,*[a] J. R. Croy,*[a] Eungje Lee,[a] A. Gutierrez,[a] Meinan He,[a] Joong Sun Park,†[a] B. T. Yonemoto,‡[a] B. R. Long,§[a] J. D. Blauwkamp,¶[a] C. S. Johnson,[a] Youngho Shin[b] and W. I. F. David[cd]

Manganese oxides, notably γ-MnO_2 and modified derivatives, have played a major role in electrochemical energy storage for well over a century. They have been used as the positive electrode in primary (single discharge) Leclanché dry cells and alkaline cells, as well as in primary and secondary (rechargeable) lithium cells with non-aqueous electrolytes. Lithiated manganese oxides, such as $LiMn_2O_4$ (spinel) and layered lithium–nickel–manganese–cobalt (NMC) oxide systems, are playing an increasing role in the development of advanced rechargeable lithium-ion batteries. These manganese-rich electrodes have both cost and environmental advantages over their nickel counterpart, NiOOH, the dominant cathode material for rechargeable nickel–cadmium and nickel–metal hydride batteries, and their cobalt counterpart, $LiCoO_2$, the dominant cathode material in lithium-ion batteries that power cell phones. An additional benefit is that tetravalent manganese can be used as a redox-active and/or stabilizing 'spectator' ion in lithiated mixed-metal oxide electrodes. This paper provides an overview of the historical development of manganese-based oxide electrode materials and structures, leading to advanced systems for lithium-ion battery technology; it updates a twenty-year old review of manganese oxides for lithium batteries. The narrative emanates largely from strategies used to design manganese oxide electrode structures at the Council for Scientific and Industrial Research, South Africa (1980–1994), Oxford University, UK (1981–1982), and Argonne National Laboratory, USA (1994–2017); it highlights the worldwide evolution of ideas and recent trends to improve the design, stability, and electrochemical capacity of structurally integrated, manganese-rich electrode materials.

Received 2nd April 2018
Accepted 9th May 2018

DOI: 10.1039/c8se00157j

rsc.li/sustainable-energy

Historical background

Manganese oxides are a structurally versatile family of compounds, existing in a wide variety of polymeric forms[1] with atomic arrangements that provide an interstitial space of one-dimensional tunnels, two-dimensional layers, or three-dimensional intersecting channels. These compounds can act as a host framework for the intercalation and de-intercalation of guest ions, such as hydrogen or lithium ions. As such, they are of interest as insertion electrodes for aqueous and non-aqueous electrochemical cells and batteries.[2,3]

In 1866, George Leclanché invented a 1.5 V Zn/MnO_2 'wet' cell, which contained a zinc anode, manganese dioxide cathode with a carbon current collector, and an ammonium chloride electrolyte solution.[4] In 1886, Carl Gassner developed a 'dry' cell in which the ammonium chloride was contained in a 'plaster of paris' paste.[4] The manganese dioxide that was commonly known at that time was nsutite, a naturally occurring manganese dioxide, simply referred to as γ-MnO_2 (ref. 1) or ε-MnO_2, depending on the quality of its X-ray diffraction (XRD) pattern.[2] Nsutite electrodes were later replaced by higher quality synthetic γ-MnO_2 products prepared by electrolytic or chemical methods. Electrolytic manganese dioxide, rather than chemically prepared manganese dioxide, is the preferred cathode material for alkaline Zn/MnO_2 cells (also 1.5 V) introduced into the battery market in the late 1960s.[5] An excellent historical account of the electrochemical reactions that occur during discharge of Zn/MnO_2 cells is provided in a review by Chabre

[a]*Electrochemical Energy Storage Department, Chemical Sciences and Engineering Division, Argonne National Laboratory, Lemont, Illinois 60439, USA. E-mail: thackeray@anl.gov*

[b]*Materials Engineering Research Facility, Energy Sciences Division, Argonne National Laboratory, Lemont, Illinois 60439, USA*

[c]*ISIS Neutron and Muon Source, Rutherford Appleton Laboratory, Harwell, OX11 0QX, UK*

[d]*Inorganic Chemistry Laboratory, University of Oxford, South Parks Road, Oxford, OX1 3QR, UK*

† Current addresses: SAFT America, Cockeysville, Maryland 21030, USA.

‡ Current addresses: Microvast Power Solutions, Inc., Orlando, Florida 32826, USA.

§ Current addresses: BASF, Beachwood, Ohio 44122, USA.

¶ Current addresses: Challenge Manufacturing, Grand Rapids, MI 49544.

and Pannetier.[2] By the 1960s, several groups had concluded that the monotonic drop in potential during discharge of the cells could be attributed to a H^+-ion insertion reaction to form MnOOH (groutite),[2,6–9] rather than a displacement or conversion reaction. Specifically, in 1966, Kozawa and Powers[10] proposed that the reaction could be described as 'a homogeneous single phase, solid state process, following previously introduced thermodynamic concepts of non-stoichiometric oxides' by Vetter in 1962.[2,11] This extensive characterization of γ-MnO_2 as an insertion electrode was the forerunner to intense research into lithium intercalation compounds in the mid-to-late 1970s, such as graphite[12–18] and the metal chalcogenides (*e.g.*, TiS_2 (ref. 19–21)). Subsequently, the metal oxides $LiCoO_2$ (ref. 22 and 23) and $LiMn_2O_4$ (ref. 24–26) would spawn the non-aqueous carbon/lithium–metal-oxide battery industry in the early 1990s.

Attempts to develop and commercialize rechargeable alkaline Zn/MnO_2 cells have not been hugely successful; the cells suffer from a poor cycle life because the reaction products cannot be fully recharged,[27–29] and the zinc dendrites that form during charge can lead to internal short circuits.[30,31] However, a recent report has indicated that Zn/MnO_2 cells can be cycled with >80% energy efficiency for more than 3000 cycles if the depth of discharge is restricted to 10%.[32]

The structural complexity of γ-MnO_2 materials is described in detail by Chabre *et al.*[2] Simplistically, γ-MnO_2 can be regarded as having a composite structure, depicted ideally in Fig. 1c, in which octahedral MnO_6 units and ('1 × 1') dimensional channels of β-MnO_2 (rutile-type structure, Fig. 1b) are intergrown with ramsdellite-MnO_2 units and channels of larger ('2 × 1') dimension (Fig. 1a). Synthetic β-MnO_2 tends to be anhydrous[33] whereas the (2 × 1) channels in ramsdellite- and γ-MnO_2 structures can be protonated or contain a minor amount of occluded water.[1,2] In practice, the arrangement of the β-MnO_2 and ramsdellite-MnO_2 building blocks in γ-MnO_2 is not ideal. The intergrown structures contain defects, stacking faults, and structural disorder that lead to XRD patterns with broad and sharp peaks, making accurate structural analysis of this family of compounds, and the differences between them, difficult.

In 1975, Ikeda disclosed a 3 V non-aqueous primary Li/γ-MnO_2 cell with a voltage double that of the aqueous Zn/MnO_2 cell,[34] which was commercialized the following year.[35] In this case, the cathode was heat-treated at 350–430 °C to remove occluded and surface water from the electrode prior to cell assembly, thereby significantly improving the electrochemical properties and life of the cell.[36] Lithium intercalation occurs predominantly in the '2 × 1' channels of the heated γ-MnO_2 structure. The '1 × 1' channels of the rutile component are small and energetically resistant to lithium uptake, consistent with the finding that, when lithiated chemically at 50 °C, β-MnO_2 transforms to spinel ($LiMn_2O_4$) to accommodate the additional lithium.[37]

Rechargeable lithium cells with pre-lithiated and heat-treated γ-MnO_2 cathodes were subsequently developed for the battery market.[38] The cathodes were prepared by reacting LiOH (or $LiNO_3$) with γ-MnO_2, typically in a 3 : 7 molar ratio at 350–430 °C, to form an intergrown electrode structure, referred to as 'composite dimensional manganese oxide' ('CDMO') by Sanyo, which was initially believed to consist of structurally connected Li_2MnO_3 (Li : Mn = 2 : 1) and lithium-stabilized γ-MnO_2 components.[39] This interpretation was later changed because a Li : Mn ratio of 3 : 7 (1 : 2.33) would thermodynamically favor the formation of a lithium–manganese-oxide spinel component at ~400 °C, such as $Li_2Mn_4O_9$ (Li : Mn = 1 : 2), rather than Li_2MnO_3, whose XRD patterns are similar.[40,41]

These studies highlighted the concept of using composite electrode structures with electrochemically active and inactive components, the former contributing to capacity generation, and the latter providing structural stability. Subsequently, this approach was further exploited in designing advanced NMC electrode structures for lithium-ion batteries.

There also are MnO_2 structures with tunnels of larger dimension, *e.g.*, '2 × 2' tunnels (hollandite), '2 × 3' tunnels (romanechite), and '3 × 3' tunnels (todorokite).[1] The structure

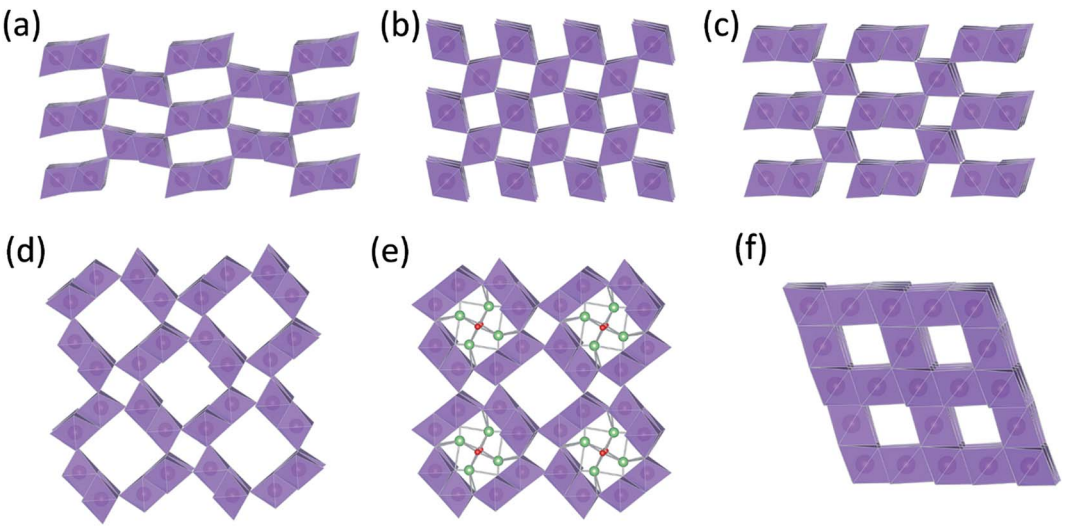

Fig. 1 MnO_2 structure types: (a) ramsdellite-MnO_2, (b) β-MnO_2 (rutile), (c) γ-MnO_2, (d) α-MnO_2 (hollandite), (e) Li_2O-stabilized α-MnO_2, and (f) λ-MnO_2 (defect spinel).

of hollandite, commonly known as α-MnO_2 (Fig. 1d), is particularly intriguing; it has the characteristic '2 × 1' MnO_6 units of ramsdellite but also the characteristic ('1 × 1') channels of β-MnO_2. The α-MnO_2 framework contains stabilizing cations within the '2 × 2' tunnels, for example, Na^+, K^+, Ca^{2+}, or Ba^{2+} ions (Fig. 1e). The α-MnO_2 structure can also be stabilized by hydronium (H_3O^+)[42] or ammonium (NH_4^+)[43] ions. In this case, negatively charged O^{2-} and N^{3-} ions are located at the center of the '2 × 2' channels, occupying at least some of the vacant sites of a distorted close-packed oxygen array;[44] the protons provide compensating positive charge within the '2 × 2' channels necessary to stabilize the structure. A recent report has provided evidence that hydrated α-MnO_2 is stabilized by both hydronium ions and water molecules.[45] The α-MnO_2 framework is zeolitic in nature; when this material is heated to 400 °C and cooled in a moist air, the water component can be reversibly removed from, and reincorporated, into the pores of the stable framework structure.[46] The protons in H_3O^+-stabilized α-MnO_2 can be ion-exchanged with lithium to yield products that provide superior capacity and electrochemical stability relative to metal-stabilized analogues (Na^+, K^+, Ca^{2+}, Ba^{2+}, *etc.*) in rechargeable 3 V Li cells.[44,47] More recently, α-MnO_2 has been identified as a promising electrocatalyst for Li-oxygen cells.[46,48] This finding begs the question whether, in a hybrid Li-ion/Li–O_2 system in which both manganese and oxygen participate in the electrochemical redox reactions, the electrocatalytic activity of α-MnO_2 is associated with the removal of lithium and oxygen ions from the '2 × 2' channels during charge, and re-accommodation during discharge.[49]

The advent of lithium-ion technology

The advent of lithium-ion batteries in 1991, with the introduction of high potential lithium–metal oxide cathodes, coupled to a carbon anode, was a game changer in the battery industry. It opened the door to the exploration, identification, and exploitation of a vast number of cathode compositions and structures.[50–52] Remarkably, $LiCoO_2$ (ref. 20) is still the cathode material of choice for the ever-expanding cell phone industry. The high cost of cobalt and the political instability of cobalt-producing countries have intensified worldwide efforts to use lithium-ion batteries with alternative cathode materials, such as nickel- and manganese-based metal oxides, for large-scale, heavy-duty batteries for hybrid and all-electric vehicles, as well as stationary energy storage for telecommunications, and back-up for the electrical grid. Partial substitution of cobalt by nickel and aluminum has provided alternative nickel-rich cathode compositions, *e.g.*, $LiNi_{0.8}Co_{0.15}Al_{0.05}O_2$ (NCA),[50,52] for high power applications such as electric vehicles. However, Ni-rich electrode materials such as NCA suffer from structural and chemical instabilities through oxygen loss above 4 V that can lead to a fast self-heating rate below 200 °C,[53] thereby compromising the safety of lithium-ion cells.[54] A concerted effort has therefore been made over the past two decades to replace or substitute cobalt and nickel in layered oxides with manganese, because lithium-ion cells with NMC cathodes offer competitive energy density and greater stability at high charging potentials (>4 V).[54]

$LiMn_2O_4$ (spinel) and substituted derivatives

Fig. 2 presents a 'compositional' phase diagram for the Li–Mn–O system, constructed in the early 1990s to emphasize compositional and oxidation state differences that affect the electrochemical behavior of spinel-related electrodes.[3,55] The diagram highlights, in particular, (i) the stoichiometric spinel tie-line between $LiMn_2O_4$ and $Li_4Mn_5O_{12}$ represented by the $Li_{1+x}Mn_{2-x}O_4$ system ($0 \leq x \leq 0.33$), (ii) the stoichiometric lithiated spinel (rock-salt) tie-line between $LiMn_3O_4$ and $Li_7Mn_5O_{12}$, and (iii) the $LiMn_2O_4$–$Li_4Mn_5O_{12}$–MnO_2 defect spinel tie-triangle, which contains, for example, λ-MnO_2 and $Li_2Mn_4O_9$.

Phase diagrams of lithium-ion electrode systems reported in the battery literature, *e.g.*, Fig. 2, can reflect metastable materials formed by lithium insertion/extraction reactions at room temperature, each of which will have its own electrochemical signature. These diagrams, therefore, do not accurately indicate the stable compositions and structures that would co-exist under isothermal conditions, particularly at the high temperatures at which parent lithium metal oxide electrodes are synthesized. For example:

(1) In Fig. 2, the stoichiometric spinels $LiMn_2O_4$ and $Li_4Mn_5O_{12}$ are typically prepared in air at 850 °C and 400 °C, respectively, while the metastable, defect-spinel λ-MnO_2 (ref. 56) and the lithiated spinels $Li_2[Mn_2]O_4$ and $Li_7[Mn_5]O_{12}$ (ref. 25 and 55) can be prepared by chemical or electrochemical methods at room temperature. On heating in an inert atmosphere, the lithiated spinel $Li_2[Mn_2]O_4$ will transform to orthorhombic $LiMnO_2$ while, on heating in air, it will transform to Li_2MnO_3 and $LiMn_2O_4$. Note also that the composition $LiMnO_2$ can have several structure types depending on the method and temperature of synthesis, for example, layered

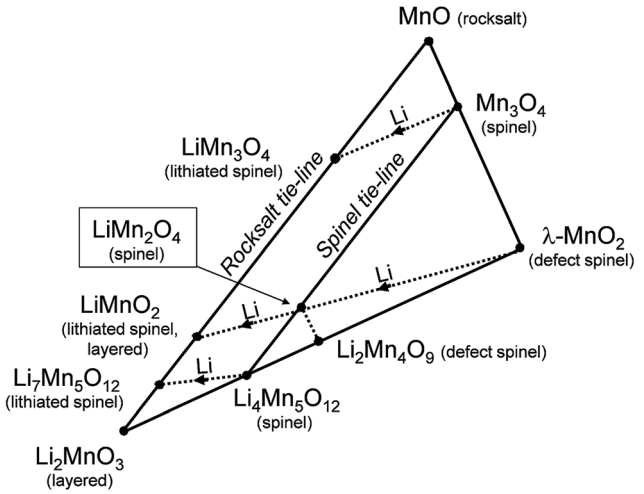

Fig. 2 Compositional Li–Mn–O phase diagram with respect to spinel, rock salt, and layered compounds (adapted from Thackeray *et al.*[55]).

(monoclinic),[57] lithiated spinel (tetragonal),[25] and staggered (orthorhombic)[58] configurations, or intergrowths between them.[57]

(2) In the Li–Co–O system, layered $LiCoO_2$ is typically prepared at about 850 °C in air, whereas a metastable structural configuration approximating the lithiated spinel $Li_2[Co_2]O_4$ (also $LiCoO_2$) is generated at 400 °C; both structure types are preserved on cooling to room temperature but display significantly different electrochemical behavior.[59–61]

Fig. 2, coupled to supporting experimental data,[25,55,62,63] underscores the following structure–electrochemical property relationships (at room temperature, ~25 °C) in lithium–manganese-oxide spinel electrodes, notably those in the stoichiometric spinel $Li_{1+x}Mn_{2-x}O_4$ ($0 \leq x \leq 0.33$) system:

(1) Lithium insertion invokes an immediate first-order transition during discharge from a spinel to a rock-salt-type structure by displacing cations from tetrahedral to octahedral sites.[25,55] This is an attractive electrochemical reaction because both spinel and rock-salt structures are found in nature and, therefore, represent intrinsically stable atomic configurations in the charged and discharged states of the electrode, respectively. In $LiMn_2O_4$ ($x = 0$), the spinel-to-rock-salt transition occurs by simultaneous lithium insertion and a two-phase conversion reaction, which results in a constant voltage discharge rather than a monotonically decreasing voltage expected for a homogeneous, single-phase (solid solution) reaction.

(2) The $Li_{1+x}Mn_{2-x}O_4$ ($0 \leq x \leq 0.33$) spinel structures on the $LiMn_2O_4$ ($x = 0$)–$Li_4Mn_5O_{12}$ ($x = 0.33$) tie-line in Fig. 2 are cubic. Lithium insertion into these structures induces a Jahn–Teller (tetragonal) distortion when the average Mn oxidation state falls below 3.5+, *i.e.*, when the Jahn–Teller active Mn^{3+} (d^4) ion concentration reaches a critical value.[55] The magnitude of the crystallographic distortion depends on the Mn^{3+}-ion concentration. For example, electrochemical lithiation of cubic $LiMn_2O_4$ (average Mn oxidation state = 3.5+; $c/a = 1$) immediately yields tetragonal $Li_2Mn_2O_4$ (average Mn oxidation state = 3.0+; $c/a = 1.16$).[25,62] On the other hand, $Li_4Mn_5O_{12}$ (average Mn oxidation state = 4.0+; $c/a = 1$) undergoes a cubic–cubic transition to yield $Li_{6.5}Mn_5O_{12}$ (average Mn oxidation state = 3.5+; $c/a = 1$) before the tetragonal phase $Li_7Mn_5O_{12}$ (average Mn oxidation state = 3.4+; $c/a = 1.11$) is formed;[55] in this case, the Jahn–Teller effect is not as pronounced as it is in $Li_2Mn_2O_4$. Note that this effect is also suppressed during the lithiation of the tetragonal spinel, Mn_3O_4 ($c/a = 1.16$); here, lithiation results in tetragonal $LiMn_3O_4$ ($c/a = 1.05$), which is close to cubic ($c/a = 1.0$), consistent with the reduction in the average Mn oxidation state from 2.67+ to 2.33+.[25]

(3) Lithium is extracted electrochemically from tetrahedral sites of the $Li_{1+x}Mn_{2-x}O_4$ spinel electrodes, such as $LiMn_2O_4$ ($x = 0$), at a potential of approximately 4 V *vs.* metallic lithium, whereas lithium is inserted into interstitial octahedral sites of the spinel structure at approximately 3 V to yield ordered rock-salt configurations.[24,62–66] Cubic–cubic transitions are reversible, whereas cubic–tetragonal transitions tend to be less so, particularly when lithium insertion induces large anisotropic changes to the unit cell parameters.[55]

Despite the advantages of low cost and electrochemical stability (safety) that manganese offers over cobalt- and nickel-rich electrodes, $LiMn_2O_4$ and substituted derivatives (LMO), such as those containing excess lithium and a little aluminum to enhance structural and electrochemical stability,[67–69] provide inferior capacity and energy output relative to $LiCoO_2$ (LCO) and $LiNi_{0.8}Co_{0.15}Al_{0.05}O_2$ (NCA) electrodes. However, manganese dissolution from LMO electrodes, which has been attributed to the disproportionation reaction $Mn^{3+} \rightarrow Mn^{4+}$ and Mn^{2+} at the particle surface,[56,70,71] severely compromises the cycle life of carbon/$LiMn_2O_4$ lithium-ion cells.[71] Nevertheless, significant progress has been made in enhancing surface stability, reducing manganese dissolution, and alleviating capacity fade through a wide variety of surface treatments.[72–77] Although LMO does not compete directly with LCO, NCA, and NMC cathodes in terms of capacity, energy output, and cycling stability, LMO has been blended with these cathode materials to offset the higher cost of cobalt and nickel.[78] The high-potential (4.7 V) $Li_xMn_{1.5}Ni_{0.5}O_4$ spinel ($0 \leq x \leq 2$) is receiving particular attention for next generation systems because it offers the possibility of significantly increasing the energy and power of a lithium-ion cell relative to an all-manganese (4.1 V) LMO cathode. Note that (1) in a standard $Li_xMn_2O_4$ electrode, the manganese ions are redox active over the full range of x ($0 \leq x \leq 2$), whereas, ideally, in well-ordered $Li_xMn_{1.5}Ni_{0.5}O_4$ electrodes, the Mn^{4+} ions are electrochemically inactive and play a spectator role that allows reversible Ni^{2+} to Ni^{4+} redox reactions to occur over the range $0 \leq x \leq 1$; and (2), for the range $1 < x \leq 2$, the damaging Jahn–Teller (Mn^{3+}) effect in $Li_xMn_{1.5}Ni_{0.5}O_4$ electrodes during lithium insertion at 3 V is not as pronounced as it is in $Li_xMn_2O_4$ electrodes, the average manganese oxidation state at the end of discharge of these two electrodes at $x = 2$ being 3.3+ and 3.0+, respectively.[25,79,80] However, to date, electrolyte instability at 4.7 V has precluded the commercialization of $LiMn_{1.5}Ni_{0.5}O_4$ spinel electrodes in Li-ion cells.

Li_2O-stabilized MnO_2 structures

Early studies of lithium–manganese-oxide spinel systems exposed the importance of lithia (Li_2O) as a stabilizing component in manganese oxide structures, in which the oxygen ions of the lithia and manganese oxide components form a close-packed oxygen array.[3] For example:

(1) Li_2O-stabilized α-MnO_2 with 1-D channels provides significantly superior electrochemical properties relative to metal cation-substituted α-MnO_2 derivatives, such as K^+-stabilized α-MnO_2.[40,44]

(2) Li_2MnO_3 ($Li_2O \cdot MnO_2$) has a Li_2O-stabilized, layered (2-D) MnO_2 rock-salt configuration, which is electrochemically inactive as an insertion electrode below ~4.5 V *vs.* metallic lithium.[3,81]

(3) The spinel $Li_4Mn_5O_{12}$, alternatively $2Li_2O \cdot 5MnO_2$, with 3-D channels for Li^+-ion transport, provides superior cycling stability to lithium insertion/extraction at 3 V relative to $LiMn_2O_4$ by mitigating the Jahn–Teller effect.[55]

Lithia also stabilizes other transition metal oxide electrode materials. For example, V_2O_5 reacts with lithia to form LiV_3O_8 ($Li_2O \cdot V_2O_5$),[82,83] which markedly improves the structural stability and electrochemical properties (*e.g.*, energy and power)

of the electrode system relative to unlithiated V_2O_5, notably in solid state lithium-polymer electrolyte cells that operate close to 100 °C.[84,85] The realization that lithia could be used effectively as a stabilizing component in metal oxides subsequently led to the design of structurally integrated electrodes and lithium-ion systems with enhanced electrochemical properties, particularly those with a Li_2MnO_3 ($Li_2O \cdot MnO_2$) component.[86,87]

Layered lithium manganese oxides and substituted derivatives

Layered manganese oxide structures, such as the minerals birnessite $[Na,Ca,Mn(^{2+})]Mn_7O_{14} \cdot 2.8H_2O$, lithiophorite $LiAl_2[Mn(^{4+})_2Mn(^{3+})]O_6(OH)_6$, and chalcophanite $ZnMn(^{4+})_3O_7 \cdot 3H_2O$, occur in nature.[1] As the formulae indicate, their structures are stabilized by metal cations, water molecules, and/or hydroxide ions. Prior to the introduction of Li-ion batteries into the market in 1991, no anhydrous layered $LiMnO_2$ analogue of $LiCoO_2$ and $LiNiO_2$ was known.

Li_2MnO_3

In the late 1980s and early 1990s, Rossouw *et al.* synthesized a layered MnO_2 structure by digesting and leaching lithium from Li_2MnO_3 (Fig. 3a), which can be represented, alternatively, in layered notation as $Li[Li_{0.33}Mn_{0.67}]O_2$.[3,88,89] Acid treatment of Li_2MnO_3 is accompanied first by the exchange of Li^+ by H^+ in the lithium layer to yield $H_{1.5}Li_{0.5}MnO_3$ (alternatively, $H[Li_{0.33}Mn_{0.67}]O_2$); during this process, the close-packed oxygen planes (*i.e.*, O3 stacking) shear to trigonal prismatic (P3) stacking.[89–91] Further acid treatment removes both lithium and oxygen from the structure to yield a layered product $(H,Li)_{2-x}MnO_{3-x/2}$ that contains both protons and residual Li^+ ions.[89] Attempts to create an anhydrous, layered structure by heating $(H,Li)_{2-x}MnO_{3-x/2}$ have been unsuccessful. The structure transforms to γ-MnO_2 under prolonged acid treatment;[92] the transformation also occurs when highly delithiated $(H,Li)_{2-x}MnO_{3-x/2}$ products are stored in air.[93]

Chemical re-lithiation of $(H,Li)_{2-x}MnO_{3-x/2}$ with LiI in acetonitrile results in the exchange of protons by lithium ions with concomitant reduction of the manganese ions to yield the composition $Li_{1.1}Mn_{0.9}O_2$;[89] discounting any remaining protons, this formula can be written, alternatively, as $0.2Li_2MnO_3 \cdot 0.8LiMnO_2$.[86] Re-lithiation of $(H,Li)_{2-x}MnO_{3-x/2}$ with LiI regenerates the close-packed oxygen array of the parent Li_2MnO_3 structure.

The electrochemical extraction of lithium from Li_2MnO_3 at 4.5 V and above was first reported by Kalyani *et al.*[94] and subsequently by the Bruce group.[81,95] The activation of a supposedly 'inactive' electrode material was attributed to the loss of oxygen that accompanied lithium extraction at high potentials with a compositional net loss of 'Li_2O' (*i.e.*, $Li_{2-x}MnO_{3-x/2}$), possibly facilitated by proton exchange. The loss of Li_2O from Li_2MnO_3 ($Li_2O \cdot MnO_2$) increases the concentration of the MnO_2 component within the structure, thereby rendering the electrode electrochemically active to lithium insertion and extraction. Electrochemically activated Li_2MnO_3 electrodes do not cycle well, presumably because, like acid-treated Li_2MnO_3 electrodes, the layered structure transforms readily to a spinel-type configuration.[81] The exploitation of oxygen redox reactions in high-capacity Li_2MnO_3-stabilized electrodes is discussed later in this paper.

The preparation of anhydrous layered $LiMnO_2$ from the isostructural sodium analogue, $NaMnO_2$, by ion exchange with Li in a non-aqueous solvent was reported in 1996 almost simultaneously by Delmas *et al.*[96] and Bruce *et al.*[57] Layered $LiMnO_2$ and substituted derivatives, such as $LiMn_{2-x}Co_xO_2$ ($0 < x \leq 0.5$), are electrochemically unstable;[97] on cycling, manganese is displaced from the Mn-rich layers to adjacent lithium-depleted layers, thereby transforming to a structure with spinel-like character, consistent with the electrochemical behavior of Li_2MnO_3.[81] The layered-to-spinel phase transition occurs *via* the disproportionation reaction:

$$2Mn^{3+} \rightarrow Mn^{4+} + Mn^{2+}$$

Trivalent Mn^{3+} ions in the octahedral sites of the manganese layer are displaced *via* tetrahedral sites, where they reside temporarily as Mn^{2+} (d^5) ions, into octahedral sites of the lithium-depleted layer before being simultaneously re-oxidized to generate localized spinel-like arrangements within a residual layered matrix.[97,98] The displacement of the manganese ions, induced by the lithium extraction process at moderately high potentials, is disadvantageous because the uncontrolled formation of a structure with intermediate layered–spinel character leads to a pronounced hysteresis in the charge/discharge profile.[97]

Layered $LiMO_2$ (M = Co, Ni, Mn)

The introduction of $LiCoO_2$ as a viable lithium-ion cathode material resulted in concerted efforts during the 1990s to

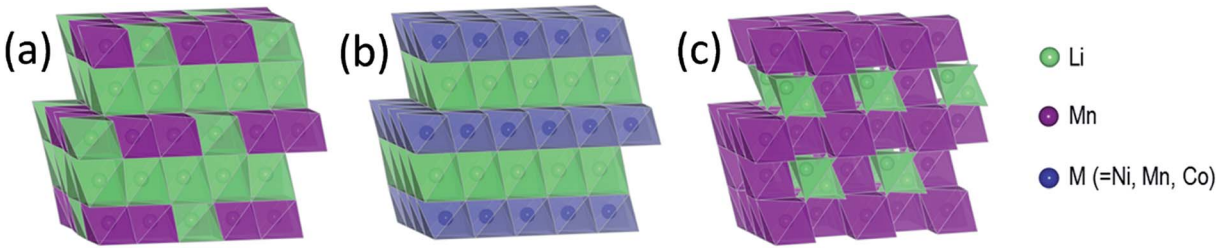

Fig. 3 Idealized close-packed structures of (a) layered Li_2MnO_3, (b) layered $LiMO_2$ (M = Co, Ni, Mn), and (c) cubic spinel $LiMn_2O_4$.

synthesize layered mixed-metal oxide electrode structures,[50] such as lithium–cobalt–nickel oxides,[99,100] lithium–manganese–nickel oxides,[101,102] lithium–manganese–cobalt oxides,[103,104] and lithium–manganese–chromium oxides.[105,106] These studies were later expanded to include ternary and higher-order transition metal oxide systems, notably NMC electrodes.

Advances in designing layered electrode structures

At present, NMC materials, $LiCoO_2$, $LiNi_{0.80}Co_{0.15}Al_{0.05}O_2$, substituted derivatives of $LiMn_2O_4$, and olivine $LiFePO_4$ (LFP),[107–109] which was discovered in 1996, constitute the dominant cathode materials in the lithium-ion battery industry. Substituted $Li_{1+x}Mn_{2-x-y}M_yO_4$ (*e.g.*, M = Al) spinel and LFP electrode structures and compositions have been optimized by industry and do not compete with layered metal oxide cathodes from a cell capacity and energy standpoint. The best opportunity for advancing lithium-ion battery cathodes, therefore, rests with layered metal oxides and, in particular, NMC materials. Nickel-rich NMC electrode materials are currently in vogue because they offer high energy and power, but are compromised by thermal instability and safety concerns at high states of charge, while layered Mn-rich NMC electrodes suffer from structural instability and low power, yet remain attractive because of their potential energy, cost, and safety advantages.

Li_2MnO_3-stabilized electrode structures

Lithium extraction from layered $LiMO_2$ electrode structures, in general, reduces the binding energy between the oxygen layers, thereby destabilizing lithium-deficient materials. Therefore, it is not surprising that phase transitions can be induced by displacing transition metal ions from their layer to sites left vacant by the exiting lithium ions in adjacent layers, or by sliding the close-packed oxygen planes to reduce the free energy of the electrode system.[81,110,111] For $Li_{1-x}CoO_2$, these damaging transitions start to occur when $x \approx 0.5$,[112] which corresponds to a capacity of approximately 140 mA h g^{-1}, whereas the transformation from layered $LiMnO_2$ to spinel $LiMn_2O_4$ occurs almost immediately with lithium extraction.[81] More lithium (*i.e.*, $x > 0.5$) can be extracted from Ni-substituted layered electrodes, such as $Li_{1-x}Ni_{0.80}Co_{0.15}Al_{0.05}O_2$ and $Li_{1-x}Ni_{0.0.33}Mn_{0.33}Co_{0.33}O_2$, in which Al and Mn play a stabilizing role, before major structural changes occur, thereby increasing the capacity and energy of the cell.[52] One concept to suppress phase transitions in layered $LiMO_2$ cathodes, and thereby enhance cell capacity and energy, is to integrate a structurally compatible, and electrochemically inactive, layered $Li_2M'O_3$ (M′ = Mn, Ti, Zr) component ($Li_2O{\cdot}M'O_2$) with the electrochemically active $LiMO_2$ component.[86,87,113–116] These materials are commonly formulated as $xLi_2M'O_3{\cdot}(1-x)LiMO_2$ to emphasize their structural components and composition. At present, systems in which M′ = Mn and M = Ni, Mn, and Co are receiving the most attention. They are also referred to as 'layered–layered' electrodes, because it is easy to follow the compositional changes during electrochemical lithium extraction/reinsertion reactions on a $xLi_2M'O_3$–$LiMO_2$–$M''O_2$ phase diagram (M″ = MM′).[86] This design concept mimics the intergrowth structure of γ-MnO_2, as discussed earlier, in which the ramsdellite-MnO_2 component is electrochemically active to lithium insertion/extraction, while the β-MnO_2 component provides structural stability and is essentially inactive to lithium uptake. For this reason, the term 'composite structure' has been used to describe 'layered–layered' Li_2MnO_3-stabilized $LiMO_2$ electrode materials.[87] Note that the 'layered–layered' formula $xLi_2MnO_3{\cdot}(1-x)LiMO_2$ can be normalized to the standard layered (rock-salt) notation $Li_{1+(x/2+x)}M'_{1+(x/(2+x))}O_2$ in which M′ = Mn + M or, more simply, $Li_{1+y}M'_{1-y}O_2$ where $y = (x/(2+x))$. Although the structures of these layered materials have also been referred to as 'solid solutions,' in reality they are inhomogeneous and highly complex.[117]

Structurally integrated cathode materials are being explored worldwide, particularly those using Li_2MnO_3 as a stabilizing component, integrated either with another structurally compatible layered component, $LiMO_2$ (M = Mn, Ni, Co), or a LiM'_2O_4 spinel component, or both. Numerous reports of the structural and electrochemical properties of these materials, both experimental and theoretical, have appeared in the literature over the past decade, many of which are cited in the references listed herein. Specifically, readers are referred to recent reviews of these materials by Croy *et al.*,[118] Passerini *et al.*,[119] Zheng *et al.*,[120] and Manthiram *et al.*[121] and to computational studies by Benedek and Iddir,[122–124] Persson *et al.*,[125,126] and Wolverton *et al.*[127] These articles provide guidance in understanding the complex structural and electrochemical features of Li_2MnO_3-based systems.

Structural considerations

Fig. 3 illustrates the idealized and well-known structures of (a) layered Li_2MnO_3, (b) layered $LiMO_2$ (M = Co, Ni, and Mn), and (c) spinel $LiMn_2O_4$, *i.e.*, the components under consideration for designing structurally integrated 'layered–layered', 'layered–spinel', and 'layered–layered–spinel' electrode materials. The $LiMn_2O_4$ spinel structure has an ideal cubic-close-packed (ccp) oxygen array, whereas the layered rock-salt structures Li_2MnO_3 (monoclinic) and $LiMO_2$ (M = Co,Ni – monoclinic, M = Mn – trigonal) deviate slightly from ideal ccp stacking. In an ideal $LiMO_2$ layered structure (Fig. 3b), trivalent M and monovalent Li ions occupy the octahedral sites in alternate layers in a 1 : 1 ratio. In Li_2MnO_3, or in layered $LiMO_2$ notation, $Li[Li_{1/3}Mn_{2/3}]O_2$ (Fig. 3a), lithium ions fully occupy the octahedral sites of one layer and share the octahedral sites in every alternate layer with tetravalent manganese ions in a 1 : 2 ratio. In $LiMn_2O_4$ (Fig. 3c), tetravalent and trivalent Mn ions (net oxidation state = 3.5+) occupy one-half of the octahedral sites; they are distributed in an ordered configuration in alternate layers in a 3 : 1 ratio, thus imparting some layered character to the spinel structure.

Fig. 4a shows the building block of Li_2MnO_3, which has been proposed to play a key role in stabilizing layered[86,87,116] and spinel[128–130] electrode structures. The lithium and manganese ions are each bonded to six oxygen ions in octahedral coordination and are ordered such that each lithium ion in the

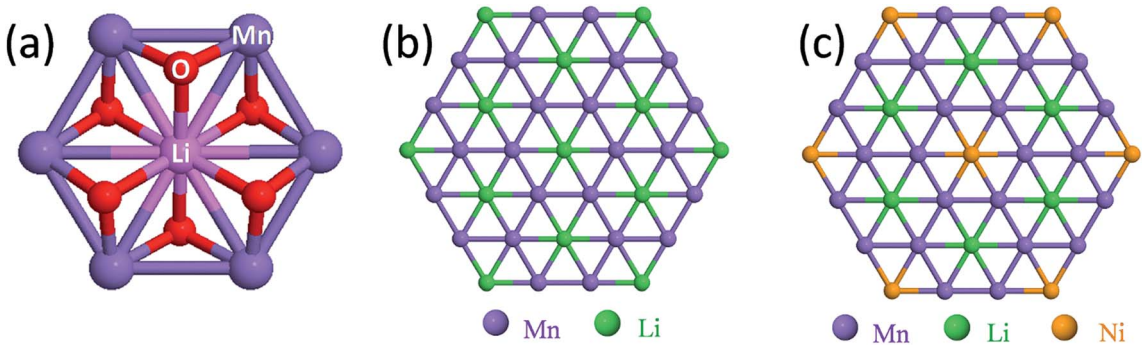

Fig. 4 (a) Characteristic $LiMn_6$ unit of Li_2MnO_3, (b, c) projections of atomic configurations in the transition-metal rich layers of ideal Li_2MnO_3 and $0.5Li_2MnO_3 \cdot 0.5LiNi_{0.5}Mn_{0.5}O_2$ structures, respectively.

manganese layer has six nearest neighbor manganese ions, as depicted by the $LiMn_6$ configurations in Fig. 4b. Fig. 4c is an idealized representation of the cation distribution in the transition metal layers of a $0.5Li_2MnO_3 \cdot 0.5LiMn_{0.5}Ni_{0.5}O_2$ electrode structure.[131] These layers consist of an interconnected array of $LiMn_6$ and $NiMn_6$ units, which represent the Li_2MnO_3 and $LiMn_{0.5}Ni_{0.5}O_2$ components of the structure, respectively (Fig. 4c). Note that in $0.5Li_2MnO_3 \cdot 0.5LiMn_{0.5}Ni_{0.5}O_2$, the manganese ions are all tetravalent while the nickel ions are divalent, as they are in layered $LiMn_{0.5}Ni_{0.5}O_2$ alone[132] and in the spinel $LiMn_{1.5}Ni_{0.5}O_4$.[133] Below ~4.5 V, all the electrochemical capacity of the electrode is derived from $Ni^{2+} \leftrightarrow Ni^{4+}$ redox reactions, while the tetravalent manganese ions act as 'spectator' ions and stabilizing agents. By contrast, in $0.5Li_2MnO_3 \cdot 0.5LiCoO_2$, the Li_2MnO_3 and $LiCoO_2$ components tend to phase segregate during synthesis,[134] forming interconnected nanodomains in a complex mosaic pattern.[135]

'Layered–layered' electrodes: the Li_2MnO_3–$LiMO_2$–MO_2 system

A compositional phase diagram of the Li_2MnO_3–$LiMO_2$–MO_2 (M = Mn, Ni, Co) system is shown in Fig. 5. The Li_2MnO_3–$LiMO_2$ tie-line represents the compositions of structurally integrated 'layered–layered' $xLi_2MnO_3 \cdot (1-x)LiMO_2$ electrode materials described in the preceding section. Lithium extraction from these materials occurs first with a concomitant oxidation of the transition metal (M) cations in the $LiMO_2$ component. During this reaction, the composition of the electrode follows the direction of the arrows away from the $xLi_2MnO_3 \cdot (1-x)LiMO_2$ tie-line. For a standard $LiCoO_2$ electrode (*i.e.*, $x = 0$, M = Co), lithium extraction follows the black arrow along the $LiMO_2$–MO_2 tie-line, which represents a continually changing electrode composition, *e.g.*, $Li_{1-x}CoO_2$, as x increases. When charged to 4.3 V, approximately one-half of the lithium ions can be extracted reversibly from $LiCoO_2$, which corresponds to a capacity of ~140 mA h g^{-1}, before the onset of structural perturbations and reactions with the electrolyte.[111,112] Slightly higher reversible capacities can be achieved from NMC electrodes when a small amount of additional lithium is added to the electrode composition.[136] These lithium-rich and manganese-containing electrodes can be represented by the notation $xLi_2MnO_3 \cdot (1-x)LiMO_2$, because the excess lithium together with some manganese can constitute the Li_2MnO_3 component of the electrode structure.[87] Lithium extraction from slightly lithium-rich NMC electrodes follows the red reaction path on the Li_2MnO_3–$LiMO_2$–MO_2 phase diagram in Fig. 5; these electrodes yield a slightly higher capacity than $LiCoO_2$, typically ~160 mA h g^{-1} when charged to 4.3 V.[136] In this instance, the Li_2MnO_3 component is electrochemically inactive

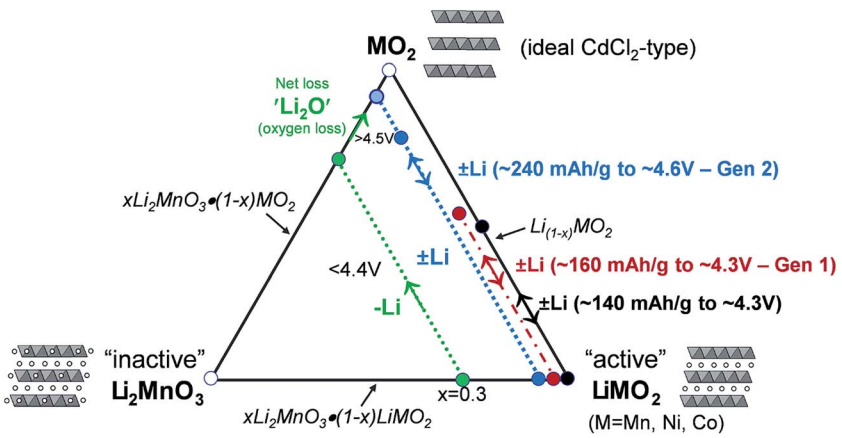

Fig. 5 Li_2MnO_3–$LiMO_2$–MO_2 compositional phase diagram (adapted from Thackeray *et al.*[86,87]).

and acts as a spectator ion and stabilizing agent, allowing extra capacity (*i.e.*, lithium) to be cycled during charge and discharge relative to stoichiometric ($LiMO_2$) NMC electrodes. Lithium-rich NMC electrodes demonstrate an enhanced rate capability, which is dependent on the relative amounts of nickel, manganese, and cobalt.[137,138]

The amount of inactive Li_2MnO_3 in the $xLi_2MnO_3\cdot(1-x)LiMO_2$ electrode increases with x. Therefore, when charged to 4.3 V, electrodes with higher values of x provide a lower capacity as indicated by the short reaction path for $x = 0.3$, highlighted in green, for complete lithium extraction from the $LiMO_2$ component, relative to the $LiMO_2$-to-MO_2 reaction (*i.e.*, $x = 0$), highlighted in black. However, for electrodes with $x = 0.3$, if charged above 4.5 V, lithium can be extracted from the Li_2MnO_3 component with a concomitant loss of oxygen (net loss Li_2O), which drives the composition of the electrode towards the MO_2 apex of the phase diagram, thereby increasing the concentration of an electrochemically active MnO_2 component in the structure, and hence the capacity of the electrode.[87,139–141] The reaction is complex, particularly during the early break-in cycles above 4.5 V. Not much gaseous oxygen is observed during lithium extraction at such high potentials,[142] which implies that some undetected oxygen may react immediately with, and oxidize, the electrolyte at the particle surface.[121] In studies of lithium-rich metal oxide electrodes at high potentials, hybridization of the transition metal d and oxygen 2p bands has been given as a reason for the oxygen redox activity.[121,143,144] Recently, Ceder *et al.* proposed that the oxygen redox capacity is also dependent on the need for particular Li–O–Li configurations within these structures.[145] The anomalously high capacity (~300 mA h g^{-1}) that can be obtained from fully activated electrodes is significantly higher than the expected theoretical value for transition metal redox reactions alone (~260 mA h g^{-1}).[114] These high capacity reactions involving oxygen are partially reversible;[146,147] however, the capacity diminishes on extended cycling, consistent with progressive oxygen loss, to values that can be attributed solely to redox reactions on the transition metal ions.

Lithium- and manganese-rich 'layered–layered' electrode structures have high capacity but are unstable when cycled repeatedly to high potentials (>4.5 V).[114,119–121,148,149] This inherent instability is not surprising, given that layered $LiMnO_2$ electrodes convert to spinel-like configurations, a process that involves the migration of manganese from the transition-metal layers to the lithium-depleted layers with the evolution of the characteristic 4 V and 3 V electrochemical signatures of a $LiMn_2O_4$ spinel electrode. Lithium- and manganese-rich $xLi_2MnO_3\cdot(1-x)LiMO_2$ electrodes, such as $0.5Li_2MnO_3\cdot 0.5LiMn_{0.375}Ni_{0.375}Co_{0.250}O_2$, exhibit a similar 'voltage fade' towards 3 V on cycling (Fig. 6) – a result of interlayer metal migration that generates a structure with a lower Gibbs free energy relative to the parent layered material. When activated at high potentials, the electrochemical properties of these complex mixed-metal oxides are also highly dependent on the electrode composition, *i.e.*, the Ni : Mn : Co ratio. For example, Long *et al.*[130] at Argonne National Laboratory have shown that the electrochemical properties of $0.25Li_2MnO_3\cdot 0.75LiMn_yNi_yCo_{1-2y}O_2$ electrodes are strongly dependent on the value of y. The cycling protocol typically adopted at Argonne to evaluate 'layered–layered' compositions and structures is to subject lithium cells initially to one formation cycle between 4.6 and 2.0 V and, thereafter, to continuous cycling between ~4.45 and ~2.50 V.[130] Capacity *vs.* cycle number plots and corresponding dQ/dV plots of a $Li/0.25Li_2MnO_3\cdot 0.75LiMn_yNi_yCo_{1-2y}O_2$ cell are provided in Fig. 7a–c and d–f, respectively. The data clearly show enhanced cycling capacity and stability, as well as the suppression of voltage fade, when the electrode has a relatively high manganese and nickel content (y) and a low cobalt content ($1-2y$).

Although synthesizing high-quality $xLi_2MnO_3\cdot(1-x)LiMO_2$ electrode materials reproducibly can be difficult, Fig. 8 highlights the electrochemical stability of a $Li/0.5Li_2MnO_3\cdot 0.5LiMn_{0.5}Ni_{0.5}O_2$ cell after activating the cathode at 4.6 V for several cycles to induce voltage fade.[150] In this instance, voltage *vs.* capacity plots of cycles 15 to 25 (*i.e.*, after electrochemical activation) and corresponding dQ/dV plots of this cell (Fig. 8a and b, respectively), cycled continuously between 4.6 and 2.0 V, show that the charge and discharge reactions are remarkably reversible during these early cycles. However, (1) the Ni reduction peak at 3.7 V is significantly weaker than it is for the relatively stable $0.25Li_2MnO_3\cdot 0.75LiMn_yNi_yCo_{1-2y}O_2$ electrode in Fig. 7c, which was charged to a slightly lower voltage limit

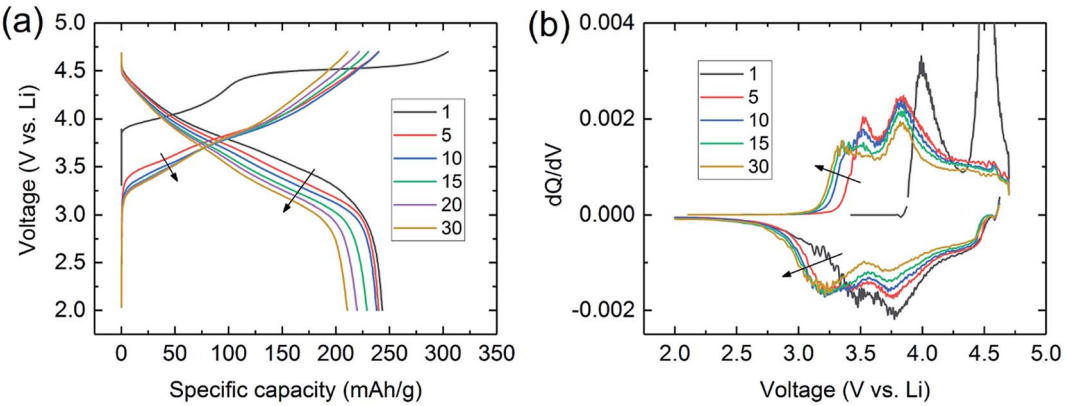

Fig. 6 (a) Voltage fade profiles and (b) corresponding dQ/dV plots during cycling of a $Li/0.5Li_2MnO_3\cdot 0.5LiMn_{0.375}Ni_{0.375}Co_{0.250}O_2$ cell.

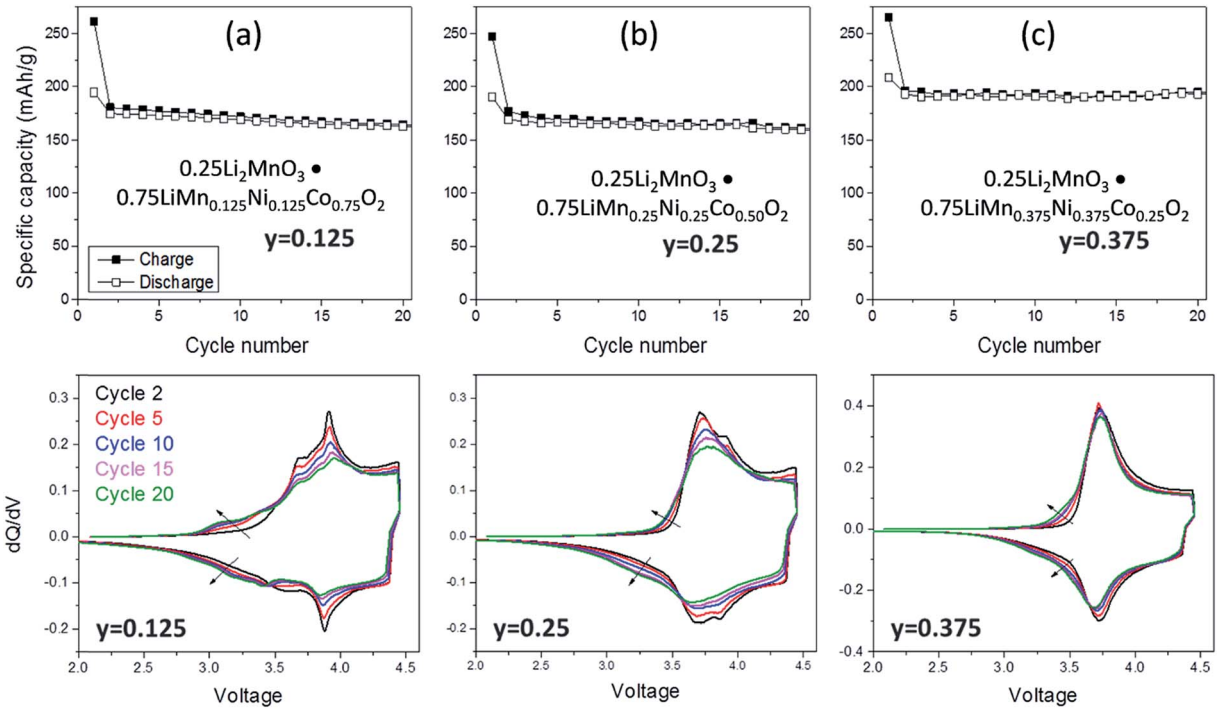

Fig. 7 Electrochemical cycling stability (top) and dQ/dV plots (bottom) of 'layered–layered' 0.25 $Li_2MnO_3 \cdot 0.75LiMn_yNi_yCo_{1-2y}O_2$ electrodes in lithium cells: (a) $y = 0.125$, (b) $y = 0.250$, and (c) $y = 0.375$ (reproduced with permission from *J. Electrochem. Soc.*, Long *et al.*[130] Copyright 2014, The Electrochemical Society).

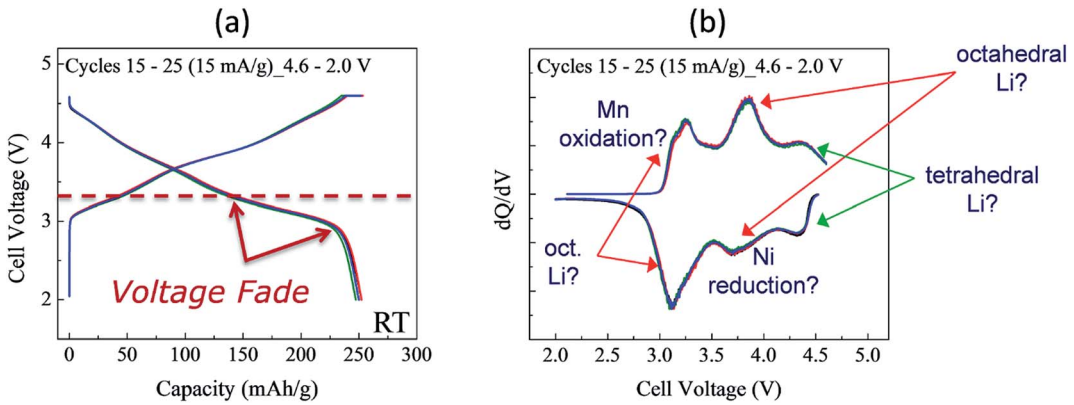

Fig. 8 Cycling stability of Li/0.5$Li_2MnO_3 \cdot 0.5LiMn_{0.5}Ni_{0.5}O_2$ cell (Mn : Ni ratio = 3 : 1): (a) voltage *vs.* capacity plots (cycles 15, 20, and 25) and (b) corresponding dQ/dV plot.

(4.45 V), and (2) most of the discharge occurs below 3.5 V. This voltage fade, which causes asymmetry in the charge and discharge profiles because of transition metal migration during lithium insertion/extraction reactions, is disadvantageous for several reasons:[151–153]

(1) it causes hysteresis in the charge/discharge process;

(2) it reduces the energy output of the cell;

(3) it increases cell impedance at both high and low states of charge, thereby lowering lithium diffusion rates (power); and

(4) it compromises the management of cells and batteries.

Despite these negative attributes, high-capacity 'layered–layered' $xLi_2MnO_3 \cdot (1-x)LiMO_2$ electrodes continue to receive worldwide attention in attempts to find ways to mitigate their limitations, particularly the suppression or elimination of transition-metal migration during electrochemical reactions when the electrodes are charged to 4.5 V and above.

Configurational considerations

The complex interconnected nanodomains observed in $0.5Li_2MnO_3 \cdot 0.5LiCoO_2$ can be addressed in simple terms by using Pauling's principle of electrostatic valence. Consider the oxygen coordination in $LiCoO_2$ and Li_2MnO_3. In $LiCoO_2$, each oxygen is surrounded by three Li^+ and three Co^{3+} ions. Given

that all cations are octahedrally coordinated by six oxygen ions, and each oxygen ion is correspondingly coordinated by six cations, and following Pauling's principle, the Li^{+}–O^{2-} and Co^{3+}–O^{2-} bonds will have formal valences of $\frac{1}{6}$ and $\frac{3}{6}$, respectively. For each oxygen, the lithium layer contributes $3 \times \frac{1}{6} = \frac{1}{2}$ summed bond valence while the Co layer contributes $3 \times \frac{3}{6} = \frac{3}{2}$. This leads to a total formal bond valence of +2, which charge balances the formal valence of O^{2-}. The situation with Li_2MnO_3 is similar except that the total $LiMn_2$ metal layer bond valence of $+\frac{3}{2}$ is the sum of $\frac{1}{6}+\frac{4}{6}+\frac{4}{6}$. This can be expressed in the rule that the sum of the formal valence of the cation triangles in the metal layer should equal 9 for charge balancing between nearest neighbor cations and anions.

To investigate cation ordering in the metal layer, a simulated annealing cation-swapping optimization algorithm, which minimizes the squared difference between 9 and the sum of every metal-triangle bond valence, was developed.[154] For a given chemical composition, cations are initially randomly placed on an extended two-dimensional hexagonal lattice. The cations are then swapped until a minimum is reached in the bond-valence cost function. For Li_2MnO_3, the signature honeycomb configuration is rapidly obtained (Fig. 4b). The results for $0.5Li_2MnO_3 \cdot 0.5LiCoO_2$ are presented in Fig. 9a, which shows nanodomain structures that are similar to those observed by Bareño *et al.*[135] Reducing the fraction of Li_2MnO_3 in $xLi_2MnO_3 \cdot (1-x)LiCoO_2$ to $x = 0.3$ results in the formula $Li(Li_{0.1}Mn_{0.2}Co_{0.7})O_2$; performing the cation-swapping optimization also produces segregated nanodomains (Fig. 9b). This segregation appears to be driven principally by the strong electrostatic preference for Li^{+} to be coordinated by two Mn^{4+} ions. Despite the simplicity of the cation-swapping algorithm, its ability to model $0.5Li_2MnO_3 \cdot 0.5LiCoO_2$ and both end members Li_2MnO_3 and $LiCoO_2$ suggests that it provides a reasonable description of the mesoscale structures of these materials and a tool to probe the configurational complexity of Li_2MnO_3-containing electrode materials.

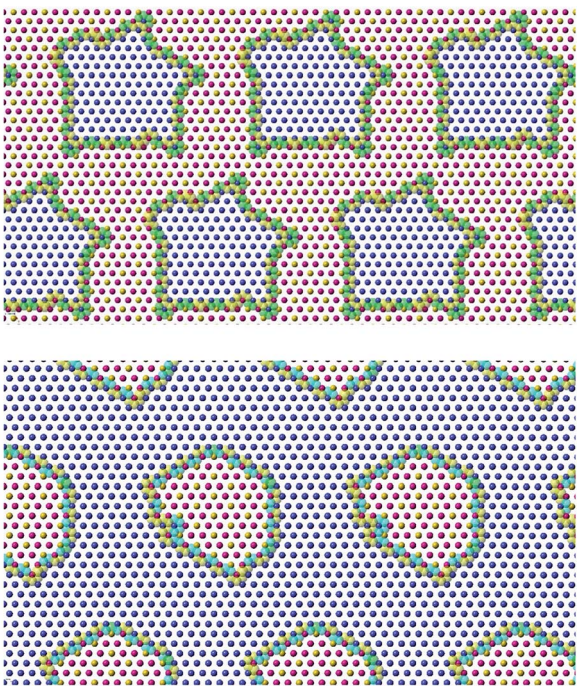

Fig. 9 Theoretical potential topological configurations of the mesoscale structure of (a) $0.5Li_2MnO_3 \cdot 0.5LiCoO_2$ and (b) $Li(Li_{0.1}Mn_{0.2}Co_{0.7})O_2$ indicating phase segregated regions of $LiCoO_2$ and Li_2MnO_3. Li^{+}, Co^{2+} and Mn^{4+} ions are illustrated as yellow, blue and pink spheres, respectively. The larger transparent yellow and green spheres respectively indicate formal charge excess and charge deficiency of the oxygen ion associated with the cation triangle. All other oxygen ions above and below the metal layer have the correct formal charge.

'Layered–layered–spinel' (LLS) electrodes: the Li_2MnO_3–$LiMO_2$–LiM'_2O_4 system

As stated above, the structural instability and voltage fade of 'layered–layered' $xLi_2MnO_3 \cdot (1-x)LiMO_2$ electrodes, when charged to potentials greater than ~4.5 V *vs.* Li^0, have been attributed predominantly to the migration of transition metals into the lithium-depleted layers during electrochemical cycling. In an attempt to address this limitation, a strategy has been adopted to fabricate $xLi_2MnO_3 \cdot (1-x)LiMO_2$ electrodes in which voltage fade is built into the electrode structures during synthesis, *i.e.*, by designing an electrode with stabilizing transition metal ions in the lithium layers of the parent material.[130,150] A seemingly logical way to achieve this is to add a spinel component to the composite 'layered–layered' structure because, unlike the two layered components that have discrete layers of lithium and transition metal ions, the transition metal cations in a LiM_2O_4 spinel component are arranged in a 3 : 1 ratio in alternate layers between ccp oxygen planes. The overall objective of the strategy, therefore, is to embed a spinel component to stabilize a 'layered–layered' structure, which is simply an extension of the concept to use a Li_2MnO_3 component to stabilize the $LiMO_2$ component in an $xLi_2MnO_3 \cdot (1-x)LiMO_2$ electrode system.[86,129]

Electrochemical delithiation of layered $LiMnO_2$ causes an internal transformation to a spinel-like structure[57,81,98] such that the spinel and layered components are structurally integrated with one another in what has been defined colloquially as a 'sp layered' configuration.[155] Note that such configurations have also recently been observed by high-resolution transmission electron microscopy (TEM) when $LiMn_2O_4$ spinel electrodes are charged to high anodic potentials.[156] In earlier studies of composite lithium–manganese-oxide materials, Rossouw *et al.* highlighted the close similarity of the XRD patterns of Li_2MnO_3 and lithia-stabilized MnO_2 materials in the $Li_2O \cdot yMnO_2$ ($y \geq 2.5$) system, such as $Li_4Mn_5O_{12}$ ($y = 2.5$) and $Li_2Mn_4O_9$ ($y = 4$).[40,157] This finding indicates that the interlayer spacing of the ccp oxygen planes is comparable in Li_2MnO_3 and spinel structures in which all the manganese ions are tetravalent, suggesting that these materials would be conducive to structural integration. Indeed, a subsequent high-resolution TEM study of the Li_2MnO_3–$Li_{1+x}Mn_{2-x}O_4$ 'layered–spinel' system revealed the remarkable structural intergrowth of Li_2MnO_3 and $Li_4Mn_5O_{12}$

($x = 0.33$) nanodomains in a $0.7Li_2MnO_3 \cdot 0.3Li_4Mn_5O_{12}$ sample synthesized at 400 °C, and a seemingly perfect alignment of the close-packed 001 and 111 oxygen planes of the layered and spinel components, respectively (Fig. 10a).[128] XRD patterns showed that heating $xLi_2MnO_3 \cdot (1 - x)Li_4Mn_5O_{12}$ materials to high temperatures in air drives the composition of the spinel component, by oxygen loss, towards $LiMn_2O_4$ ($x = 0$) in the Li–Mn–O phase diagram (Fig. 2). During this process, the cubic lattice parameter of the spinel component, a, expands with increasing Mn^{3+} concentration, as expected (Fig. 10b). The changing Li : Mn ratio in the spinel component along the $Li_4Mn_5O_{12}$–$LiMn_2O_4$ tie-line is accommodated during heat treatment by adjusting the amount of Li_2MnO_3 in the final composite structure.[128] Electrochemical charge and discharge profiles of a $Li/0.7Li_2MnO_3 \cdot 0.3Li_4Mn_5O_{12}$ half-cell confirmed the dual layered-spinel character of the cathode material. When cycled between 5.0 and 2.0 V, the capacity delivered during the initial discharge is 270 mA h g^{-1} (Fig. 10c).[128] On subsequent cycling, the electrode continued to provide more than 250 mA h g^{-1}, but lost capacity steadily, an unsurprising result given the high cutoff voltage. Note that the charge capacity on the initial cycle (252 mA h g^{-1} in Fig. 10c), which includes some electrolyte oxidation at high potentials, is smaller than the discharge capacity (270 mA h g^{-1}) because the $Li_4Mn_5O_{12}$ component in the parent electrode is in a fully charged state and, therefore, can accommodate lithium from the metallic lithium anode to yield the fully lithiated spinel composition ($Li_7Mn_5O_{12}$) during discharge at ~3 V. In a full cell configuration, $C_6/0.7Li_2MnO_3 \cdot 0.3Li_4Mn_5O_{12}$, lithium from the Li_2MnO_3 component can, therefore, serve to load the graphite anode during the electrochemical activation process, thereby countering or even eliminating first-cycle irreversible capacity losses.[158]

A compositional phase diagram of a three-component Li_2MnO_3–$LiMO_2$–LiM'_2O_4 ('layered–layered–spinel') system shown in Fig. 11 highlights the wide compositional space that exists to exploit structurally integrated layered and spinel electrode materials. The Li_2MnO_3–$LiMO_2$ tie-line reflects the composition of 'layered–layered' electrodes described in the preceding sections. Reducing the lithium content in the parent Li_2MnO_3–$LiMO_2$ electrode material necessarily drives the composition of the electrode within the tie-triangle towards the spinel apex of the triangle. This strategy has been exploited to induce the formation of a stabilizing spinel component within layered or 'layered–layered' electrode structures during synthesis at elevated temperature.[129,130]

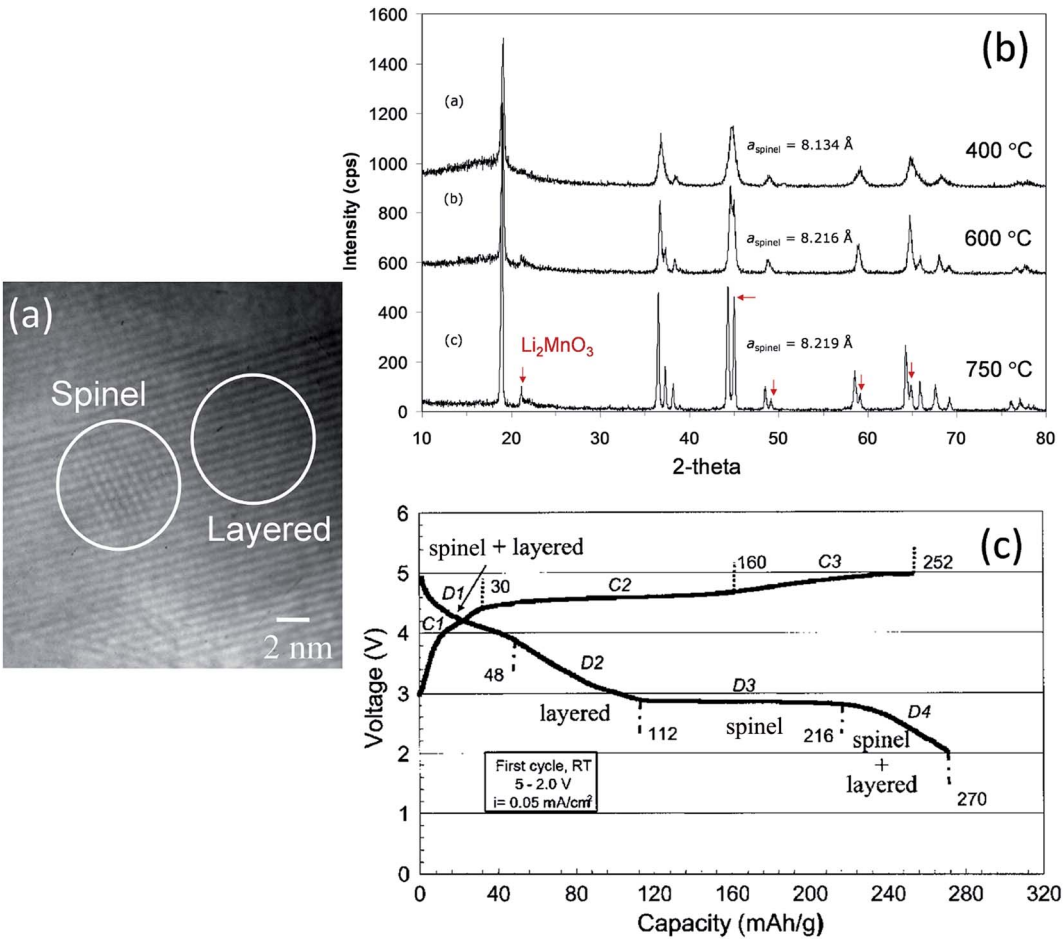

Fig. 10 (a) TEM image of $0.7Li_2MnO_3 \cdot 0.3Li_4Mn_5O_{12}$ prepared at 400 °C, (b) XRD patterns of $0.7Li_2MnO_3 \cdot 0.3Li_4Mn_5O_{12}$ (Li : Mn = 1.2 : 1) as a function of synthesis temperature, and (c) voltage profile of a $Li/0.7Li_2MnO_3 \cdot 0.3Li_4Mn_5O_{12}$ (750 °C) cell on initial charge–discharge cycle (reproduced with permission from *Electrochemical Communications*, Johnson *et al.*[128]).

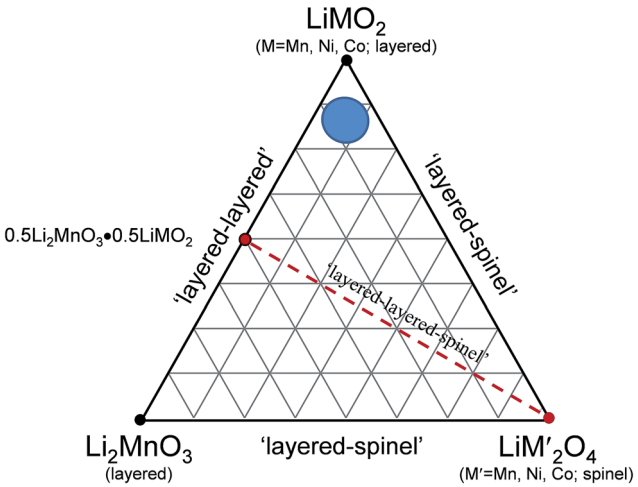

Fig. 11 Conceptual design space of a Li_2MnO_3 (layered)–$LiMO_2$ (layered)–LiM'_2O_4 (spinel) compositional phase diagram highlighting the 'layered–layered–spinel' tie-line (in red) between $0.5Li_2MnO_3$-$\cdot 0.5LiMO_2$ and LiM'_2O_4 and a region within the phase diagram representing low concentrations of stabilizing Li_2MnO_3 and LiM'_2O_4 components (in blue).

For example, reducing the amount of lithium required to synthesize Li_2MnO_3 and heating lithium-deficient precursors, $Li_{2-x}MnO_\delta$ ($0 \leq x \leq 1.5$), at 850 °C in air induces the formation of $LiMn_2O_4$, which requires some oxygen loss (δ) for charge compensation, as shown by XRD patterns (Fig. 12a) and the electrochemical profiles of $Li/Li_{2-x}MnO_\delta$ cells for $x = 0$, 0.5, 1.0, and 1.5 (Fig. 12b)[159] (note that this system can be represented, alternatively, as $yLi_2MnO_3 \cdot (1-y)LiMn_2O_4$ for $y = 0$, 0.2, 0.5, and 1.0, respectively). For $x = 1$ (*i.e.*, $0.5Li_2MnO_3 \cdot 0.5LiMn_2O_4$), a TEM image of the product shows structurally integrated Li_2MnO_3 and $LiMn_2O_4$ domains, as expected, with the spinel component residing predominantly at the surface of the particles (Fig. 12c). Unlike the TEM image in Fig. 10a, which shows a Li_2MnO_3–$Li_4Mn_5O_{12}$ composite structure synthesized at 400 °C with near perfect alignment of the close-packed planes of the two components, the image of the Li_2MnO_3–$LiMn_2O_4$ product in Fig. 12c shows a convoluted structure, which can likely be attributed to a mismatch in the lattice parameters and *d*-spacings of the layered Li_2MnO_3 and spinel $LiMn_2O_4$ components and to stacking fault disorder.

Reducing the lithium content in the 'layered–layered' composition, $0.5Li_2MnO_3 \cdot 0.5LiMn_{0.5}Ni_{0.5}O_2$ (in normalized notation $Li_{1.5}Mn_{0.75}Ni_{0.25}O_{2.5}$, or $Li_{1.2}Mn_{0.6}Ni_{0.2}O_2$), shows similar layered–spinel behavior as the $Li_{2-x}MnO_\delta$ system, described above. Increasing the lithium deficiency drives the composition of the electrode during high temperature synthesis towards the spinel composition $LiMn_{1.5}Ni_{0.5}O_4$ because the Mn : Ni ratio (3 : 1) remains constant on the $0.5Li_2MnO_3$-$\cdot 0.5LiMn_{0.5}Ni_{0.5}O_2$–$LiMn_{1.5}Ni_{0.5}O_4$ tie-line.[129] X-ray diffraction data and electrochemical profiles confirm increasing spinel-like character as the Li : transition metal ratio in the parent 'layered–layered' electrode is reduced from $x = 1$ to $x = 0$ in $x(Li_2MnO_3 \cdot 0.5LiMn_{0.5}Ni_{0.5}O_2) \cdot (1-x)LiMn_{1.5}Ni_{0.5}O_4$.[129]

A study by Long *et al.* of the compositional, structural, and electrochemical features of spinel-stabilized 'layered–layered'

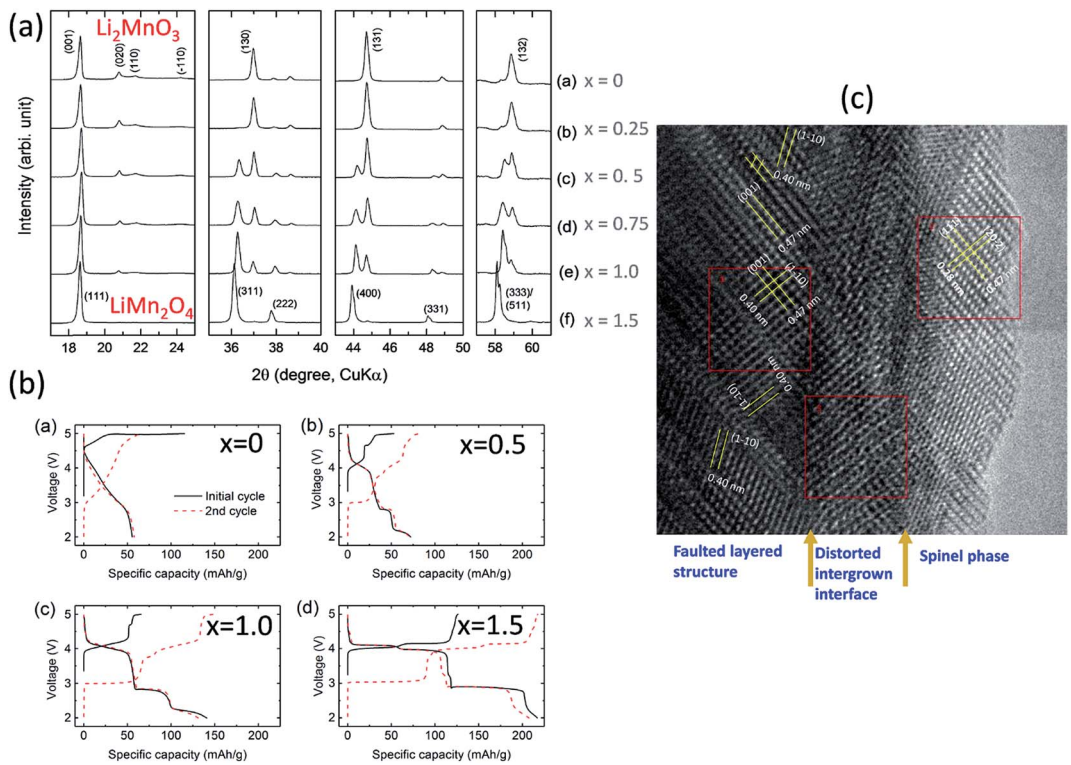

Fig. 12 Effects of reducing the Li content in $Li_{2-x}MnO_\delta$ materials after heating to 850 °C: (a) XRD data, (b) electrochemical data, and (c) TEM image of $Li_{2-x}MnO_\delta$ ($x = 1.0$).

xLi$_2$MnO$_3$·(1 − x)LiMO$_2$ (M = Mn, Ni, Co) electrodes has revealed intriguing features of 'layered–layered–spinel' electrode materials.[130] Compounds in the xLi$_2$MnO$_3$·(1 − x)LiMn$_y$Ni$_y$Co$_{1-2y}$O$_2$ system for $x = 0.25$ and $x = 0.33$ were selected for this study. The cobalt content, $1 - 2y$, was varied over the range $0.125 \leq y \leq 0.375$ while keeping a constant Mn : Ni ratio of 1 : 1. 'Layered–layered–spinel' products with a targeted spinel content of 6%, 15%, and 25% were synthesized from metal oxalate precursors by reducing the Li content in a parent 'layered–layered' composition by the appropriate amount. Fig. 13 shows, for $x = 0.25$ and $y = 0.375$, the impact of reducing the lithium content on the electrochemical capacity (in mA h g^{-1}) after an initial 'activation' charge to 4.6 V and subsequent discharge to 2.0 V. Also shown is the first-cycle efficiency. The capacity of the parent 0.25Li$_2$MnO$_3$·0.75LiMn$_{0.375}$Ni$_{0.375}$Co$_{0.250}$O$_2$ electrode (in normalized notation, Li$_{1.25}$Mn$_{0.531}$Ni$_{0.281}$Co$_{0.187}$O$_{2.25}$) increases from 208 to 212 mA h g^{-1} when the amount of lithium in the parent electrode is reduced to target a 6% spinel content. Increasing the targeted spinel content results in a decline in capacity, but it increases the first-cycle efficiency because, unlike a discharged layered LiMO$_2$ component, a charged spinel component (*e.g.*, Li$_{1+x}$Mn$_{2-x}$O$_4$) in the parent electrode can accommodate one lithium ion per formula unit. This electrochemical behavior is consistent with reports of other lithium- and manganese-rich 'layered–layered–spinel' electrode compositions.[129,130,160]

With the above-mentioned electrochemical data in mind, the current strategy at Argonne National Laboratory is to use a bottom-up strategy to develop 'layered–layered–spinel' materials that can deliver a stable capacity of at least 200 mA h g^{-1} when cycled below 4.5 V, which would make them competitive with layered Ni-rich systems.[150] Approaches are being sought to overcome electrode surface and electrolyte instabilities and capacity fade (for example, by using effective surface coatings), which would allow 'layered–layered–spinel' electrodes, when charged repeatedly to 4.6 V, to deliver close to their theoretical capacity based on the redox reactions of the transition metal ions alone (~250 mA h g^{-1}).

The impact of lowering the lithium content in 'layered–layered' electrodes on their capacity, cycling stability, and rate performance is highlighted in Fig. 14.[150] For these experiments, lithium-deficient 0.25Li$_2$MnO$_3$·0.75LiMn$_{0.375}$Ni$_{0.375}$Co$_{0.250}$O$_2$ materials were prepared at Argonne's Materials Engineering and Research Facility to target a spinel content of 2, 5, 10, and 15% in the 'layered–layered–spinel' products. Lithium coin cells containing these materials were activated on the initial charge/discharge cycle (4.6–2.0 V) and subsequently cycled between 4.45 and 2.0 V at a low rate (15 mA g^{-1}; ~C/12). Fig. 14a shows that a maximum capacity is obtained when the targeted spinel content is 5–10%, consistent with the capacity *vs.* composition plot of cells with 0.25Li$_2$MnO$_3$·0.75LiMn$_{0.375}$Ni$_{0.375}$Co$_{0.250}$O$_2$ electrodes (Fig. 13). Fig. 14a also highlights the large decline in capacity for electrodes with 15% spinel content, and the poor capacity retention on cycling for electrodes with 2% spinel content. Of particular significance is that electrodes with 5–10% spinel are also more tolerant to higher rates than the 2% spinel electrode (Fig. 14b). This finding suggests that the spinel component may reside predominantly at the surface of the 'layered–layered–spinel' electrode particles, thereby stabilizing the electrode/electrolyte interface and providing good capacity retention on long-term cycling (275 cycles, Fig. 14c).

As shown in Fig. 15a and b, high-resolution (synchrotron) XRD and TEM data of a 'layered–layered–spinel' product with a targeted 15% spinel content, derived from a lithium-deficient 0.25Li$_2$MnO$_3$·0.75LiMn$_{0.375}$Ni$_{0.375}$Co$_{0.250}$O$_2$ parent composition, provided unequivocal evidence of a spinel component embedded within the layered structure (Fig. 15a and b).[130] Of particular significance is that elemental mapping of the sample (Fig. 15c) by electron energy loss spectroscopy (EELS) indicated that regions rich in Mn and Ni adopt a spinel configuration, while regions rich in cobalt have a layered configuration. The data emphasize the complexity and inhomogeneity of these materials and the tendency to form thermodynamically favored configurations or to phase segregate on cooling the samples from the high temperature at which they are synthesized (typically 850–900 °C) to room temperature, consistent with data reported by Bareno *et al.*[135] and Long *et al.*[134] for 'layered–layered' electrodes in the Li$_2$MnO$_3$–LiCoO$_2$ system. A question that remains to be answered is: when synthesizing 'layered–layered–spinel' structures, at what lithium concentration do the transition metal ions start diffusing into the lithium-rich layers to provide a spinel character to the electrode structure, rather than maintain a layered configuration in which the lithium deficiency is compensated by oxidation state changes on the transition metal ions? In this respect, recent structural refinements of lithium-deficient 0.25Li$_2$MnO$_3$·0.75LiMn$_{0.375}$Ni$_{0.375}$Co$_{0.250}$O$_2$ electrodes with synchrotron XRD data have revealed that reducing the lithium content does not immediately induce spinel formation. The lattice parameter of the cubic spinel component that ultimately forms is 8.145 Å, which is coincidentally close to that expected for lithium–manganese-oxide

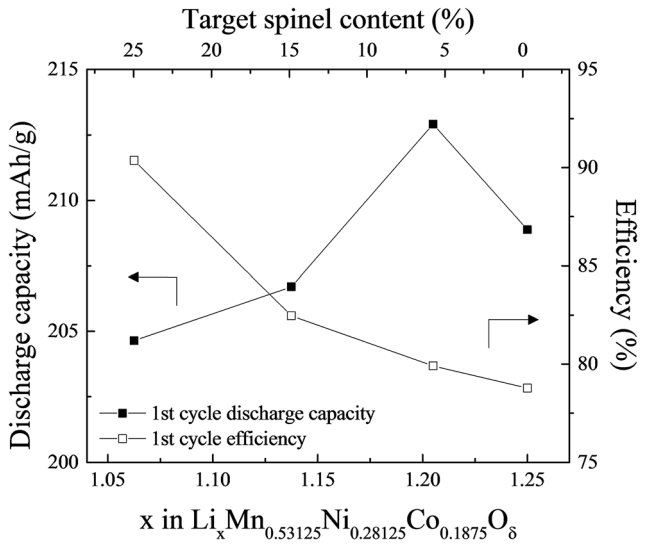

Fig. 13 The effect of varying the lithium content in 0.25Li$_2$MnO$_3$·0.75LiMn$_{0.375}$Ni$_{0.375}$Co$_{0.250}$O$_2$, *i.e.*, x in Li$_x$Mn$_{0.531}$Ni$_{0.281}$Co$_{0.188}$O$_\delta$ (reproduced with permission from *J. Electrochem. Soc.*, Long *et al.*[130] Copyright 2014, The Electrochemical Society).

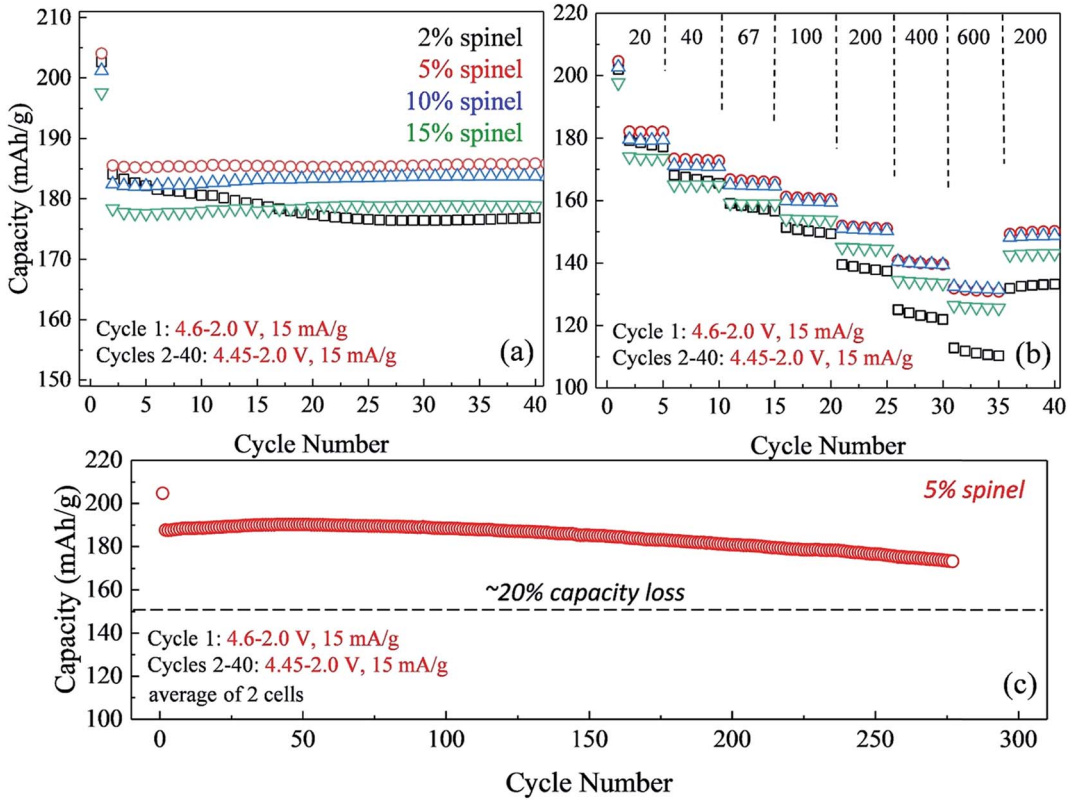

Fig. 14 (a) Cycling stability (40 cycles) and (b) rate performance of 'layered–layered–spinel' electrodes derived from a $0.25Li_2MnO_3 \cdot 0.75LiMn_{0.375}Ni_{0.375}Co_{0.250}O_2$ parent compound by reducing the lithium content to target a spinel content of 2%, 5%, 10%, and 15%; (c) cycling stability (275 cycles) of an electrode with a targeted 5% spinel content.

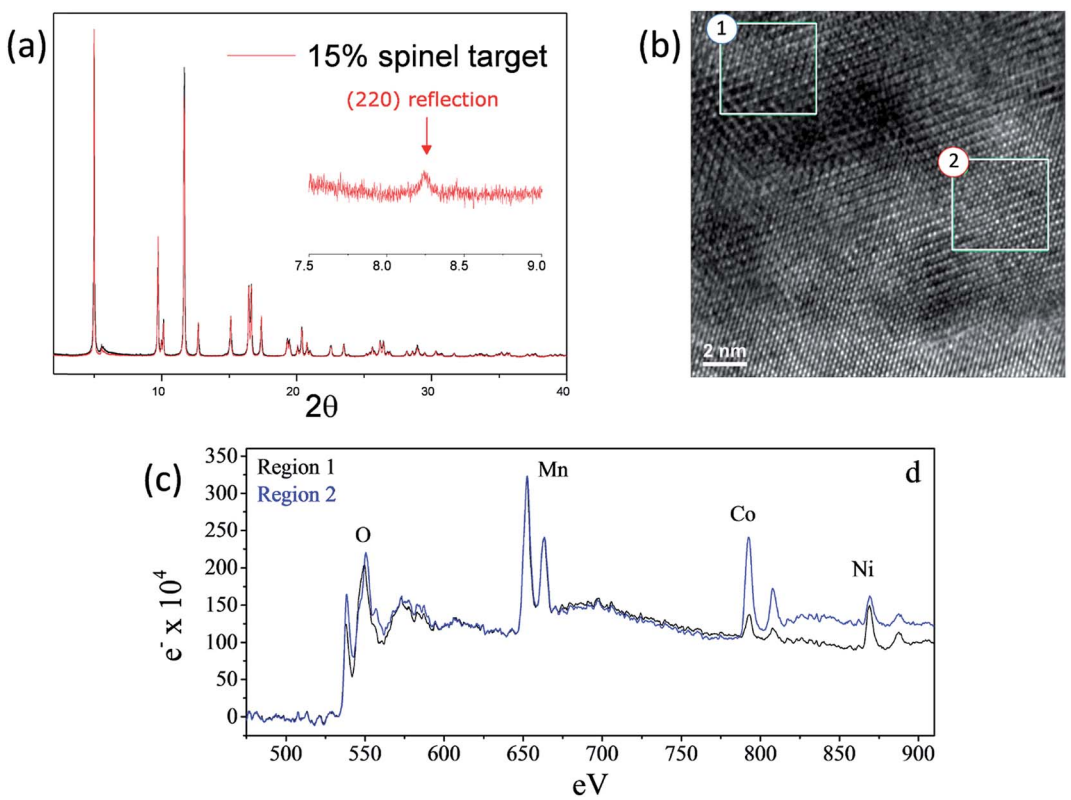

Fig. 15 (a) High-resolution XRD pattern, (b) TEM image, and (c) EELS data of a lithium-deficient $0.25Li_2MnO_3 \cdot 0.75LiMn_{0.375}Ni_{0.375}Co_{0.250}O_2$ electrode targeting 15% spinel content (reproduced with permission from *J. Electrochem. Soc.*, Long *et al.*[130] Copyright 2014, The Electrochemical Society).

spinels, such as $Li_4Mn_5O_{12}$,[55] and probably cobalt- and/or nickel-substituted derivatives.[161]

Coatings and surface treatments

The formation of protective solid-electrolyte interphase (SEI) layers at the surface of lithium-ion battery electrodes that function outside the stability window of organic electrolyte solvents, particularly lithiated graphite (LiC_6) anodes that operate at a potential of ~100 mV above metallic lithium, is a well-known and studied phenomenon;[162] without it, lithium-ion cells would not work. Unprotected lithium–metal-oxide cathodes that are electrochemically active above the upper stability limit of the electrolyte (~4 V *vs.* Li^0) also tend to suffer from interfacial electrode/electrolyte side reactions. These reactions can lead to structural decay, metal dissolution, oxygen loss, lower capacity, a slower electrochemical reaction rate, and reduced operating life, all of which can severely compromise the energy and power output of a lithium-ion cell. Numerous materials have been tried and tested as protective coatings for lithium–metal-oxide cathodes,[163] many of which, for example, Al_2O_3,[73,164] AlF_3,[165] ZrO_2,[166] Li_2ZrO_3,[167] $AlPO_4$,[168,169] $LiNiPO_4$,[170] and graphene,[77] can counter the above limitations to various extents.

'Layered–layered–spinel' electrodes derived from a parent composition $0.25Li_2MnO_3 \cdot 0.75LiMn_{0.375}Ni_{0.375}Co_{0.250}O_2$, when activated between 4.6 and 2 V, and subsequently cycled between 4.45 and 2.5 V at 15 mA g^{-1}, also benefit from surface treatment. Fig. 16 shows the electrochemical charge and discharge profiles of the first 10 cycles (top) and the 40th to 50th cycles (bottom) of lithium half cells with (a) a layered–layered $0.25Li_2MnO_3 \cdot 0.75LiMn_{0.375}Ni_{0.375}Co_{0.250}O_2$ electrode, (b) an untreated 'layered–layered–spinel' electrode with a targeted spinel content of 10% (based on inductively coupled plasma atomic emission spectroscopy (ICP-AES) analysis of the Li content), and (c) the 'layered–layered–spinel' electrode in (b) after a proprietary surface treatment. Despite several formation cycles required to stabilize the electrode reaction (Fig. 16a–c, top), all cells cycle thereafter with excellent capacity retention, with maximum capacity (~215 mA h g^{-1}) being generated by the surface-treated 'layered–layered–spinel' electrode (Fig. 16c, bottom). Note the distinct discontinuity (arrows) in the electrochemical profiles of cells containing the 'layered–layered–spinel' electrodes, tentatively attributed to structural and/or polarization effects, which could serve as an early end-of-life indicator for the cell.

Corresponding dQ/dV plots (Fig. 17) of the voltage–capacity data in Fig. 16 confirm the excellent cycling stability of untreated and surface-treated 'layered–layered' and 'layered–layered–spinel' electrodes derived from $0.25Li_2MnO_3 \cdot 0.75LiMn_{0.375}Ni_{0.375}Co_{0.250}O_2$. What is noteworthy about the dQ/dV plots is:

(1) there is significantly less hysteresis and voltage fade than for the cell containing a 'layered–layered' cathode with higher lithium and manganese content, $0.5Li_2MnO_3 \cdot 0.5LiMn_{0.375}Ni_{0.375}Co_{0.250}O_2$ (Fig. 6);

(2) the Ni redox peak at approximately 3.7 V remains stable; and

(3) the small amount of capacity generated by voltage fade during the early cycles is delivered over a wide voltage range (approximately 3.4 to 2.7 V), implying that lithium insertion takes place in a highly complex 'layered–spinel' structure in which the interstitial site energies vary widely.

Nickel-rich layered electrode materials

Nickel-rich, layered electrodes, such as NCA ($LiNi_{0.8}Co_{0.15}Al_{0.05}O_2$) and NMC analogues $LiNi_{0.8}Mn_{0.1}Co_{0.1}O_2$ ('811') and $LiNi_{0.6}Mn_{0.2}Co_{0.2}O_2$ ('622'), are currently considered next generation lithium-ion cathode materials.[54,171] Gradient

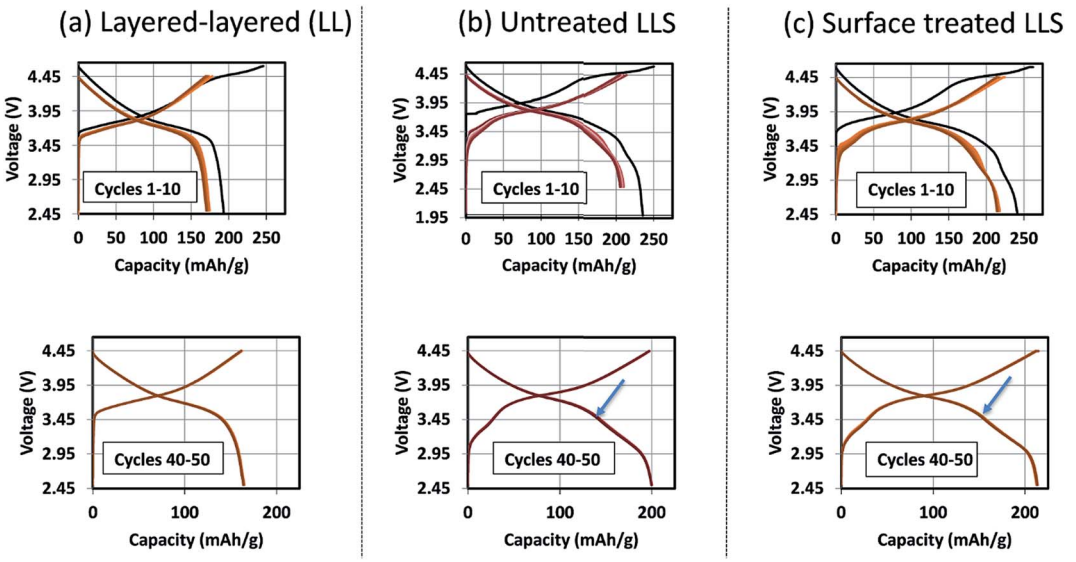

Fig. 16 Electrochemical cycling stability of untreated and surface-treated 'layered–layered' and 'layered–layered–spinel' electrodes derived from a parent composition $0.25Li_2MnO_3 \cdot 0.75LiMn_{0.375}Ni_{0.375}Co_{0.250}O_2$.

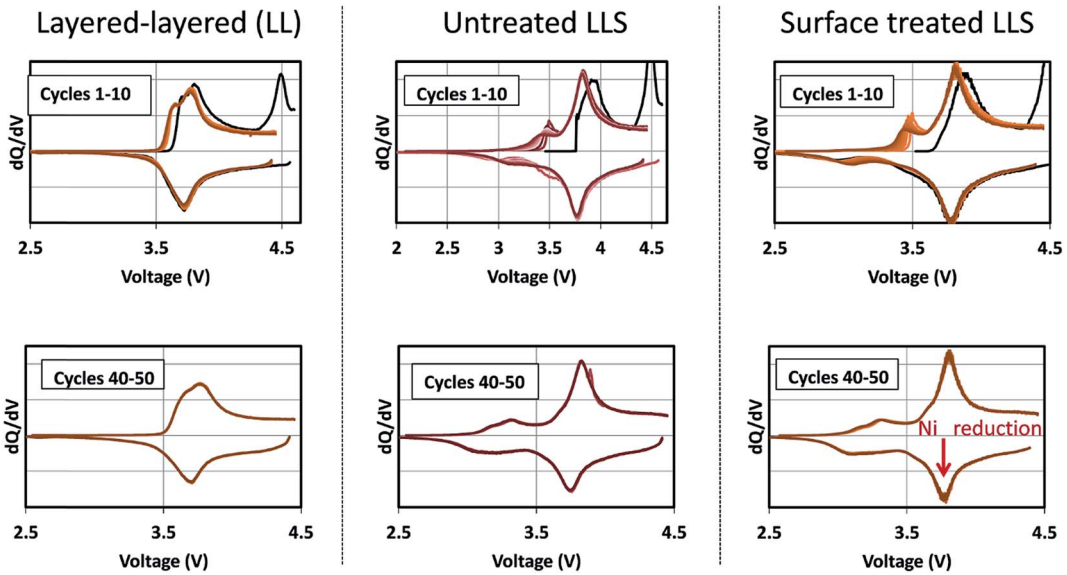

Fig. 17 Corresponding dQ/dV plots of the voltage–capacity plots in Fig. 16, highlighting the electrochemical cycling stability of untreated and surface-treated 'layered–layered' and 'layered–layered–spinel' electrodes derived from $0.25Li_2MnO_3 \cdot 0.75LiMn_{0.375}Ni_{0.375}Co_{0.250}O_2$.

cathode designs, in which a high concentration of nickel decreases from the bulk to the surface of NMC particles are also being developed.[172] However, the instability of tetravalent nickel and the possible release of oxygen in these electrodes at the top of charge introduce a safety risk, which can be reduced by increasing the manganese content. The electrochemical performance of a commercial, moderately nickel-rich NMC electrode, $LiNi_{0.5}Mn_{0.3}Co_{0.2}O_2$ ('532'), was therefore compared with a moderately manganese-rich LLS 'MNC' electrode to assess their relative electrochemical behavior, the latter product being derived from a 'layered–layered' composition $0.25Li_2MnO_3 \cdot 0.75LiMn_{0.375}Ni_{0.375}Co_{0.250}O_2$ with a targeted 10% spinel content in which the Mn : Ni : Co ratio is 5.3 : 2.8 : 1.9, *i.e.*, close to '532' (Fig. 18).[173] In these tests, the nickel-rich Li/NMC cells were charged and discharged continuously between 4.45 and 2.5 V, whereas the manganese-rich Li/MNC cells (referenced as LLS in Fig. 18) were subjected to one activation cycle between 4.6 and 2.0 V, before continuous cycling between 4.45 and 2.5 V. Cells were cycled at a 15 mA g^{-1} rate and at 30 °C.

Fig. 18a shows the first-cycle electrochemical profiles of the Li/NMC and Li/MNC (LLS) cells described above. The voltage profile of the NMC cell is consistent with a layered nickel-rich cathode structure, delivering approximately 190 mA h g^{-1} on the initial discharge. By contrast, the initial discharge capacity of the manganese-rich LLS cathode is considerably higher (238 mA h g^{-1}), the additional capacity below 3.5 V being generated by the spinel-like component within the composite electrode structure. The electrochemical profiles of the Li/NMC and Li/MNC for cycles 2 and 50 are shown in Fig. 18b and c, respectively. Despite the more pronounced voltage fade of the manganese-rich LLS electrode, Li/MNC cells outperformed their nickel-rich NMC counterpart, both in terms of capacity and energy output. More specifically, the manganese-rich LLS electrodes delivered more than 200 mA h g^{-1} and an energy output of more than 750 W h kg^{-1} (based on the mass of the cathode alone) after 50 cycles, whereas the layered nickel-rich cathodes provided approximately 180 mA h g^{-1} and less than 700 W h kg^{-1}, respectively. This result augurs well for further progress in exploiting manganese-rich LLS technology.

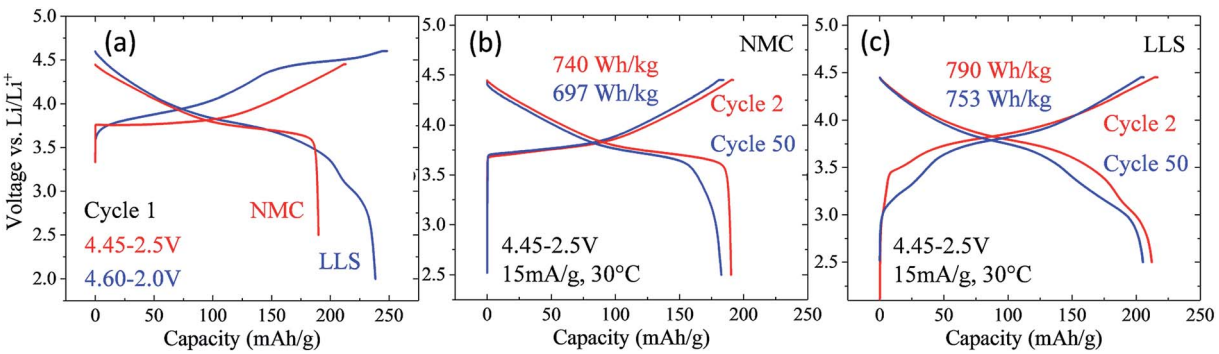

Fig. 18 Electrochemical profiles and properties of a commercial, nickel-rich layered '532' NMC electrode with a manganese-rich 'layered–layered–spinel' MNC (532) electrode with targeted spinel content of ~8%.

New approaches and future directions

Exploiting lithiated spinels as stabilizers for Li_2MnO_3–$LiMO_2$ electrodes

Despite the advances that have been made in developing manganese-rich LLS electrode materials, Fig. 18 indicates that a LLS MNC '532' electrode with 50% Mn still suffers from some structural decay and voltage fade on long term cycling. These limitations are thought to arise because MNC '532' electrodes are not as effective in arresting transition metal migration as their layered nickel- and cobalt-rich counterparts. A recent strategy that has been adopted at Argonne to address this challenge is to use a cobalt-based lithiated spinel composition $Li_2[Co_{2-2x}M_{2x}]O_4$ (*e.g.*, M = Ni, Al), alternatively $LiCo_{1-x}M_xO_2$, rather than a stoichiometric, manganese-rich spinel, to stabilize high-capacity 'layered–layered' $xLi_2MnO_3\cdot(1-x)LiMO_2$ electrodes.[174] This approach is attractive for several reasons:

(1) Like $xLi_2MnO_3\cdot(1-x)LiMO_2$ materials, lithiated spinels $Li_2[Co_{2-2x}M_{2x}]O_4$ have close-packed structures with a rock-salt stoichiometry, making them compositionally, and potentially structurally, compatible with one another.

(2) Relative to manganese and nickel, cobalt has a lower propensity to migrate in a ccp oxygen lattice,[103,175] thereby offering the possibility of mitigating voltage fade.

(3) Lithium extraction from a lithiated cobalt-rich spinel component, $Li_{2-\delta}[Co_{2-2x}M_{2x}]O_4$, occurs at a significantly higher potential (~3.6 V) than a lithiated manganese-oxide spinel analogue, $Li_{2-\delta}Mn_2O_4$ (~2.9 V).

Limited research has been conducted on lithiated cobalt spinel materials, and substituted derivatives, since their discovery in the early 1990s.[59,176] They are synthesized at a relatively low temperature (~400 °C). The lithiated spinel $Li_2[Co_2]O_4$ (or simply $LiCoO_2$) has cubic symmetry ($Fd\bar{3}m$) while its layered analogue has trigonal symmetry, $R\bar{3}m$ (Fig. 19). Some of these early structural analyses of $Li_2[Co_2]O_4$ were misleading because it had not been recognized that the atomic vector space of a cubic lithiated spinel structure is identical to that of a (hypothetical) layered $LiCoO_2$ structure in which the oxygen array is ideally cubic-close-packed.[60,61,177] In such an instance, the XRD patterns of a cubic lithiated spinel, $Li_2[Co_2]O_4$, and a cubic layered $LiCoO_2$ structure would be indistinguishable from one another, as shown in Fig. 19b and c.[60] In practice, however, layered $LiCoO_2$ deviates slightly from ideal cubic close packing, yielding a c/a ratio of 4.99, whereas cubic $Li_2[Co_2]O_4$ has the ideal c/a ratio of 4.90 for a ccp structure;[177] this difference separates the trigonal and cubic diffraction peaks from one another. Recent synchrotron XRD data and analyses have, however, confirmed the earlier conclusions that $LiCoO_2$ prepared at 400 °C (LT-$LiCoO_2$) has both layered- and lithiated-spinel character, and that 10% nickel substitution for cobalt (LT-$LiCo_{0.9}Ni_{0.1}O_2$) essentially eliminates the layered $LiCoO_2$ component from the structure (Fig. 20).[174] Recent studies at Argonne have shown that other substituents such as Al can improve the cycling stability of these materials considerably; it has also been shown that Ni-substituted spinels can react with Li_2MnO_3 to form a series of $xLi_2MnO_3\cdot(1-x)LiCo_{1-y}Ni_yO_2$ compounds ($0 \le x \le 0.2$; $0 \le y \le 0.2$), and that their electrochemical cycling stability is highly dependent on the values of x and y (Fig. 21).[178] These cobalt-rich materials, in which the surplus lithium in the transition metal layer of the Li_2MnO_3 component and the cobalt in the lithium-rich layer of the lithiated spinel component play a stabilizing role, are under investigation as possible agents for minimizing the voltage fade and capacity loss of high-capacity, manganese-rich $xLi_2MnO_3\cdot(1-x)LiMO_2$ (MNC) electrodes to an industrially acceptable level.

Exploiting oxygen redox reactions in high-capacity Li_2MnO_3-stabilized electrodes

It is now well known that anomalously high capacities can be derived from lithium- and manganese-rich electrodes by activating the electrodes through oxygen loss at potentials above

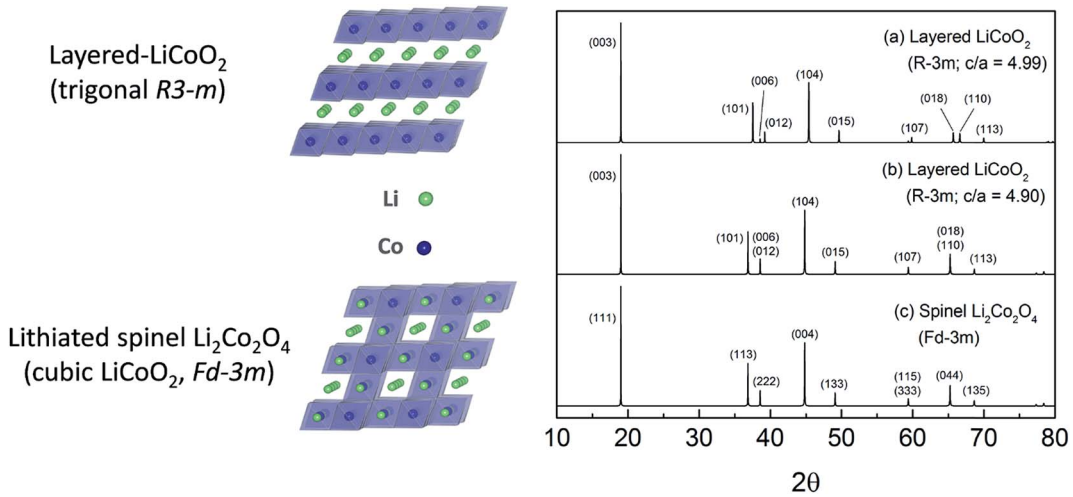

Fig. 19 Layered–spinel $LiCoO_2$ structural anomaly: simulated XRD patterns of (a) layered-$LiCoO_2$ structure ($R\bar{3}m$, $c/a = 4.99$), (b) hypothetical layered structure with ideal cubic-close-packed oxygen array ($R\bar{3}m$, $c/a = 4.90$), and (c) a cubic lithiated spinel, $Li_2[Co_2]O_4$ ($Fd\bar{3}m$), showing identical patterns to those of (b) and (c) (reproduced with permission from *ACS Appl. Mater. Interfaces*, Lee *et al.*[174]).

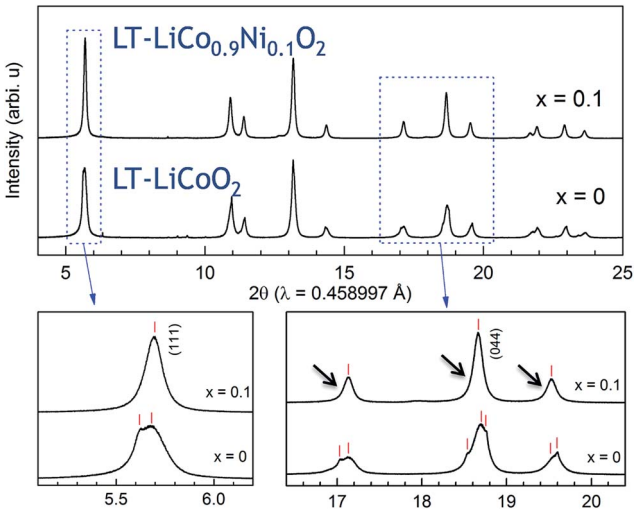

Fig. 20 Synchrotron XRD patterns of LT-$LiCo_{1-x}Ni_xO_2$ ($x = 0$ and 0.1) (reproduced with permission from *ACS Appl. Mater. Interfaces*, Lee *et al.*[174]).

4.5 V, as described earlier.[139–142] Intensive studies have been undertaken in recent years to understand and exploit electrochemically induced oxygen redox reactions in lithium metal oxides, such as Li_2MO_3 ($Li_2O{\cdot}MO_2$) (M = Ru, Ir),[143,179–181] Li_5FeO_4 ($5Li_2O{\cdot}Fe_2O_3$),[182,183] and $xLi_2MnO_3{\cdot}(1-x)LiMO_2$ (alternatively, $x[Li_2O{\cdot}MnO_2]{\cdot}(1-x)LiMO_2$) materials,[123,124,184] all of which can be regarded as having Li_2O-stabilized structures. Although some reversible (O_2^{n-}) redox behavior has been observed in these materials, it can push the structural stability of the electrode to the limit such that there is competition between the O^{2-}/O_2^{2-} anionic redox reaction and oxygen loss (O_2), particularly at the electrode surface. It has been reported that oxygen loss is preceded by a shortening of the O–O bond in Li_2IrO_3,[143] while first principles molecular dynamics simulations predict that O–O dimerization occurs in $xLi_2MnO_3{\cdot}(1-x)LiMO_2$ systems.[124] Both processes would result in a displacement of the oxygen ions from their close-packed positions in the parent electrode structure. In this respect, a recent XRD refinement of a $0.4Li_2MnO_3{\cdot}0.6LiMn_{0.5}Ni_{0.5}O_2$ electrode using synchrotron data (Fig. 22a) revealed that, on the initial charge of

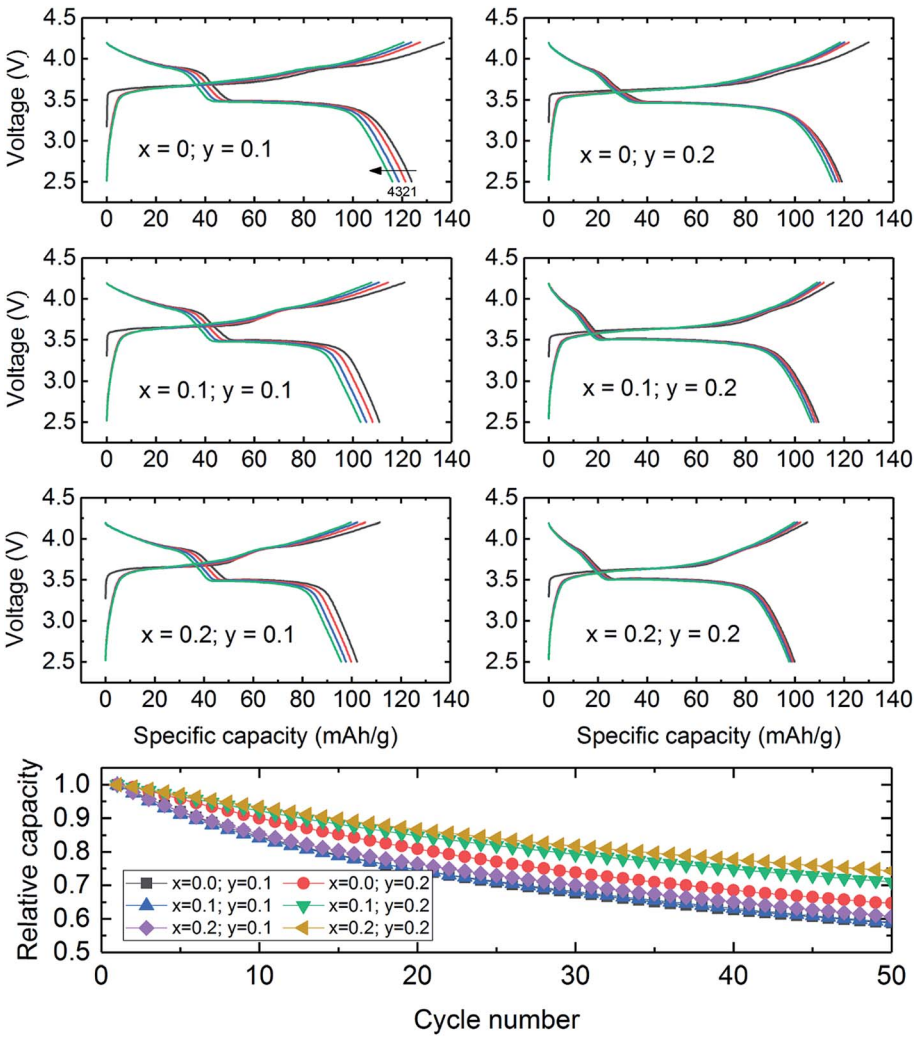

Fig. 21 Voltage profiles of 'layered–spinel' Li/$xLi_2MnO_3{\cdot}(1-x)LiCo_{1-y}Ni_yO_2$ cells ($0 \le x \le 0.2$; $0 \le y \le 0.2$) cycled between 2.5 and 4.2 V *vs.* Li at a current rate of 15 mA g^{-1}.

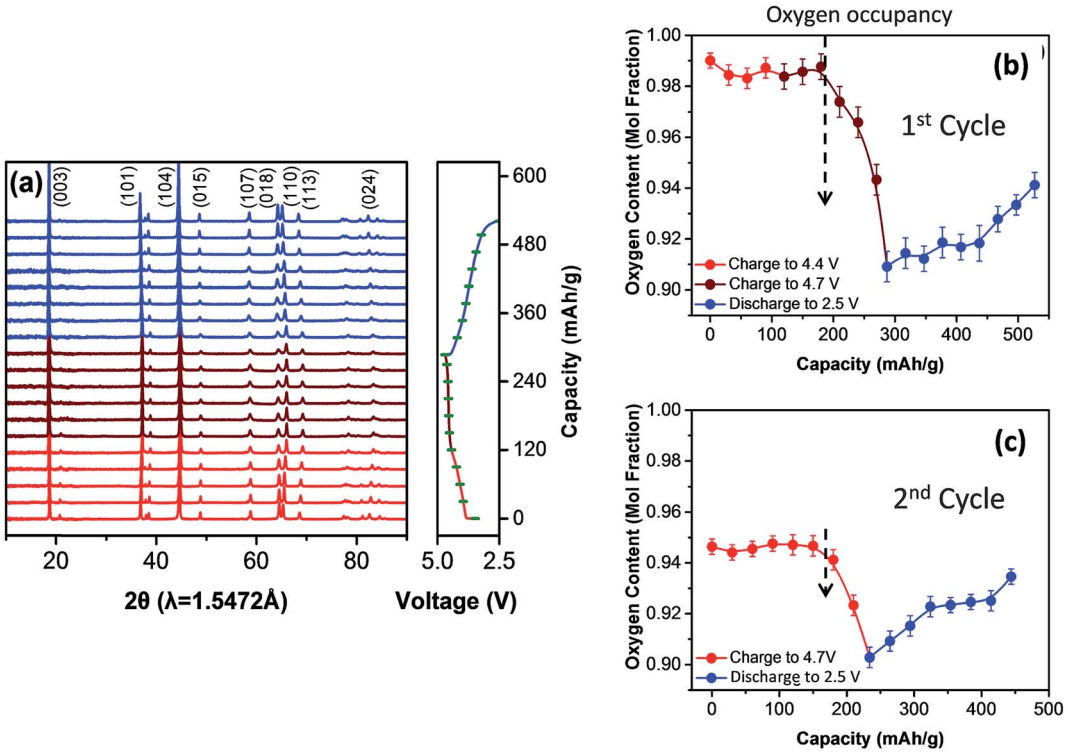

Fig. 22 (a) Synchrotron XRD data and (b, c) variation of the oxygen site occupancy in a $0.4Li_2MnO_3 \cdot 0.6LiMn_{0.5}Ni_{0.5}O_2$ electrode during the first two cycles of a lithium cell when charged and discharged between 4.7 and 2.5 V (reproduced with permission from *Nano Energy*, Yoon *et al.*[147]).

a $Li/0.4Li_2MnO_3 \cdot 0.6LiMn_{0.5}Ni_{0.5}O_2$ cell to 4.7 V, the oxygen site occupancy decreased from 0.99 after ~200 mA h g^{-1} of capacity had been withdrawn from the electrode (Fig. 22b) to 0.91 at the top of charge (~280 mA h g^{-1}), and that on the subsequent discharge to 2.5 V the site occupancy increased from 0.91 to ~0.95.[147] Similar behavior was observed on the second cycle (Fig. 22c) with improved coulombic efficiency. The study also revealed that diffraction peaks characteristic of the Li_2MnO_3 component disappeared during the initial charge and reappeared during discharge, consistent with changes in Mn–O correlations (observed by X-ray absorption spectroscopy) and a partially reversible lithium and oxygen displacement process. The data provide some hope that, with time, control of these anionic redox processes may become possible and lead to the successful exploitation of reversible oxygen electrochemistry, even if only to a limited extent, in lithium-ion cathode technology.

Concluding remarks

Today's lithium-ion battery cathodes are dominated by cobalt- and nickel-rich materials, such as $LiCoO_2$ (LCO) and $LiNi_{0.8}Co_{0.15}Al_{0.05}O_2$ (NCA), whereas manganese-based systems, such as the spinel $LiMn_2O_4$ (LMO) and $LiNi_{0.33}Mn_{0.33}Co_{0.0.33}O_2$ (NMC) play a relatively minor role in the market. Advances in cathode performance and cell energy density are likely to be made incrementally by improving the composition and structural design of lithium–metal-oxide materials and stabilized surfaces. Nickel-rich cathodes, such as NCA and NMC (*e.g.*, '811' and '622'), are currently in vogue but suffer from high cost and have potential safety concerns relative to manganese-rich materials. On the other hand, manganese-based cathodes such as $LiMn_2O_4$ and NMC ('333') will continue to serve the market, notably in the transportation sector for all-electric and hybrid-electric vehicles. The need to buffer cost when the prices of cobalt and nickel fluctuate to high values motivates and justifies further R&D of the manganese-rich high-voltage spinel, $LiMn_{1.5}Ni_{0.5}O_4$, and lithium- and manganese-rich (Li_2MnO_3-stabilized) materials such as the 'layered–layered' and 'layered–layered–spinel' systems discussed in this paper.

Statement of contributions

M. M. Thackeray – main author of this review and contributor to all aspects herein. J. R. Croy – co-author of text and author/contributor to data presented in Fig. 4, 7, 8, 13, 14–20. E. Lee – co-author of text and author/contributor to data presented in Fig. 1, 3, 6, 12, 19–21. A. Gutierrez – co-author and contributor/author to data presented in Fig. 16–18. M. He – co-author and contributor/author to data presented in Fig. 16–18. J.-S. Park – co-author and contributor/author to data presented in Fig. 6, 7, 11, 13–15, and 19. B. T. Yonemoto – co-author and contributor/author to data presented in Fig. 11, 14, 16, and 17. B. R. Long – co-author and contributor/author to data presented in Fig. 3, 7, 13–15. J. D. Blauwkamp – co-author and contributor/author to data presented in Fig. 12, 19–21. C. S. Johnson – co-author and contributor/author to data presented in Fig. 1, 2, 5, and 10. Y. Shin – co-author and contributor/author to data presented in

Fig. 14, 16, and 18. W. I. F. David – co-author and sole author of the work presented in Fig. 9.

Conflicts of interest

There are no conflicts of interest to declare.

Acknowledgements

Support from the Office of Vehicle Technologies of the U.S. Department of Energy, particularly from Tien Duong, David Howell, and Peter Faguy is gratefully acknowledged. The submitted manuscript has been created by UChicago Argonne, LLC, Operator of Argonne National Laboratory ("Argonne"). Argonne, a U.S. Department of Energy Office of Science laboratory, is operated under Contract No. DE-AC02-06CH11357. The U.S. Government retains for itself, and others acting on its behalf, a paid-up, nonexclusive, irrevocable worldwide license in said article to reproduce, prepare derivative works, distribute copies to the public, and perform publicly and display publicly, by or on behalf of the Government.

References

1 J. E. Post, *Proc. Natl. Acad. Sci. U. S. A.*, 1999, **96**, 3447–3454.
2 Y. Chabre and J. Pannetier, *Prog. Solid State Chem.*, 1995, **23**, 1–130.
3 M. M. Thackeray, *Prog. Solid State Chem.*, 1997, **25**, 1–71.
4 D. Linden and T. B. Reddy, *Handbook of Batteries*, McGraw-Hill, New York, 3rd edn, 2001.
5 P. A. Marsal, K. Kordesch and L. F. Urry, *US Pat.*, 2960558, 1960.
6 J. Brenet and P. Malessan, *C. R. Acad. Sci.*, 1956, **242**, 3064–3066.
7 K. Neumann and W. Fink, *Z. Elektrochem.*, 1958, **62**, 114–122.
8 W. C. Vosburgh, *J. Electrochem. Soc.*, 1959, **106**, 839.
9 P. Brouillet, A. Grund, F. Jolas and R. Mellet, *C. R. Acad. Sci.*, 1963, **257**, 3390.
10 A. Kozawa and R. A. Powers, *J. Electrochem. Soc.*, 1966, **113**, 870–878.
11 K. J. Vetter, *Z. Elektrochem.*, 1962, **66**, 577–586.
12 J. O. Besenhard, *Carbon*, 1976, **14**, 111–115.
13 M. Zanini, S. Basu and J. E. Fischer, *Carbon*, 1978, **16**, 211–212.
14 S. Basu, C. Zeller, P. J. Flanders, C. D. Fuerst, W. D. Johnson and J. E. Fischer, *Mater. Sci. Eng.*, 1979, **38**, 275–283.
15 M. S. Dresselhaus and G. Dresselhaus, *Adv. Phys.*, 1981, **30**, 139–326.
16 H. Ikeda, K. Narukawa and H. Nakashima, Jpn. Pat., 57-208079, 1982.
17 S. Basu, *US Pat.*, 4304825, 1981.
18 S. Basu, *US Pat.*, 4423125, 1983.
19 M. S. Whittingham, *US Pat.*, 4009052, 1977.
20 M. S. Whittingham, *Science*, 1976, **192**, 1126–1127.
21 M. S. Whittingham, *Prog. Solid State Chem.*, 1978, **12**, 41–99.
22 J. B. Goodenough and K. Mizuchima, *US Pat.*, 4302518, 1981.
23 K. Mizushima, P. C. Jones, P. J. Wiseman and J. B. Goodenough, *Mater. Res. Bull.*, 1980, **15**, 783–789.
24 M. M. Thackeray and J. B. Goodenough, *US Pat.*, 4507371, 1983.
25 M. M. Thackeray, W. I. F. David, P. G. Bruce and J. B. Goodenough, *Mater. Res. Bull.*, 1983, **18**, 461–472.
26 M. M. Thackeray, P. J. Johnson, L. A. de Picciotto, P. G. Bruce and J. B. Goodenough, *Mater. Res. Bull.*, 1984, **19**, 179–187.
27 K. Kordesch, J. Gsellmann, M. Peri, K. Tomantschger and R. Chemelli, *Electrochim. Acta*, 1981, **26**, 1495–1504.
28 R. Patrice, B. Gerand, J. B. Leriche, L. Seguin, E. Wang, R. Moses, K. Brandt and J. M. Tarascon, *J. Electrochem. Soc.*, 2001, **148**, A448–A455.
29 M. A. Dzieciuch, N. Gupta and H. S. Wroblowa, *J. Electrochem. Soc.*, 1988, **135**, 2415–2418.
30 F. R. McLarnon and E. J. Cairns, *J. Electrochem. Soc.*, 1991, **138**, 645–664.
31 T. C. Adler, F. R. Mclarnon and E. J. Cairns, *J. Electrochem. Soc.*, 1993, **140**, 289–294.
32 N. D. Ingale, J. W. Gallaway, M. Nyce, A. Couzis and S. Banerjee, *J. Power Sources*, 2015, **276**, 7–18.
33 T. Hirai and I. Tari, *Prog. Batteries Sol. Cells*, 1980, **3**, 157.
34 H. Ikeda, T. Saito and H. Tamura, *Proc. Manganese Dioxide Symposium*, 1975, vol. 1, p. 384.
35 R. J. Brodd, A. Kozawa and K. V. Kordesch, *J. Electrochem. Soc.*, 1978, **125**, C271–C283.
36 H. Ikeda, M. Hara and S. Narukawa, *US Pat.*, 4133856, 1979.
37 W. I. F. David, M. M. Thackeray, P. G. Bruce and J. B. Goodenough, *Mater. Res. Bull.*, 1984, **19**, 99–106.
38 T. Nohma, T. Saito, N. Furukawa and H. Ikeda, *J. Power Sources*, 1989, **26**, 389–396.
39 T. Nohma, Y. Yamamoto, K. Nishio, I. Nakane and N. Furukawa, *J. Power Sources*, 1990, **32**, 373–379.
40 M. M. Thackeray, M. H. Rossouw, A. de Kock, A. P. de la Harpe, R. J. Gummow, K. Pearce and D. C. Liles, *J. Power Sources*, 1993, **43–44**, 289–300.
41 E. Levi, E. Zinigrad, H. Teller, M. D. Levi, D. Aurbach, E. Mengeritsky, E. Elster, P. Dan, E. Granot and H. Yamin, *J. Electrochem. Soc.*, 1997, **144**, 4133–4141.
42 M. H. Rossouw, D. C. Liles, M. M. Thackeray, W. I. F. David and S. Hull, *Mater. Res. Bull.*, 1992, **27**, 221–230.
43 P. Botkovitz, P. Deniard, M. Tournoux and R. Brec, *J. Power Sources*, 1993, **44**, 657–665.
44 C. S. Johnson, D. W. Dees, M. F. Mansuetto, M. M. Thackeray, D. R. Vissers, D. Argyriou, C. K. Loong and L. Christensen, *J. Power Sources*, 1997, **68**, 570–577.
45 Z. Z. Yang, D. C. Ford, J. S. Park, Y. Ren, S. Kim, H. Kim, T. T. Fister, M. K. Y. Chan and M. M. Thackeray, *Chem. Mater.*, 2017, **29**, 1507–1517.
46 Z. Z. Yang, L. Trahey, Y. Ren, M. K. Y. Chan, C. K. Lin, J. Okasinski and M. M. Thackeray, *J. Mater. Chem. A*, 2015, **3**, 7389–7398.
47 M. H. Rossouw and M. M. Thackeray, *US Pat.*, 5166012, 1992.

48 A. Debart, A. J. Paterson, J. Bao and P. G. Bruce, *Angew. Chem., Int. Ed.*, 2008, **47**, 4521–4524.
49 M. M. Thackeray, M. K. Y. Chan, L. Trahey, S. Kirklin and C. Wolverton, *J. Phys. Chem. Lett.*, 2013, **4**, 3607–3611.
50 M. S. Whittingham, *Chem. Rev.*, 2004, **104**, 4271–4301.
51 J. B. Goodenough and Y. Kim, *Chem. Mater.*, 2010, **22**, 587–603.
52 N. Nitta, F. X. Wu, J. T. Lee and G. Yushin, *Mater. Today*, 2015, **18**, 252–264.
53 M. Brand, S. Glaser, J. Geder, S. Menacher, S. Obpacher, A. Jossen and D. Quinger, *2013 World Electric Vehicle Symposium and Exhibition (EVS27)*, Barcelona, Spain, 2013.
54 A. Manthiram, B. Song and W. Li, *Energy Storage Materials*, 2017, **6**, 125–139.
55 M. M. Thackeray, A. Dekock, M. H. Rossouw, D. Liles, R. Bittihn and D. Hoge, *J. Electrochem. Soc.*, 1992, **139**, 363–366.
56 J. C. Hunter, *J. Solid State Chem.*, 1981, **39**, 142–147.
57 A. R. Armstrong and P. G. Bruce, *Nature*, 1996, **381**, 499–500.
58 R. J. Gummow, D. C. Liles and M. M. Thackeray, *Mater. Res. Bull.*, 1993, **28**, 1249–1256.
59 R. J. Gummow and M. M. Thackeray, *Solid State Ionics*, 1992, **53**, 681–687.
60 E. Rossen, J. N. Reimers and J. R. Dahn, *Solid State Ionics*, 1993, **62**, 53–60.
61 R. J. Gummow, D. C. Liles and M. M. Thackeray, *Mater. Res. Bull.*, 1993, **28**, 235–246.
62 J. B. Goodenough, M. M. Thackeray, W. I. F. David and P. G. Bruce, *Rev. Chim. Miner.*, 1984, **21**, 435–455.
63 T. Ohzuku, M. Kitagawa and T. Hirai, *J. Electrochem. Soc.*, 1990, **137**, 769–775.
64 C. Masquelier, M. Tabuchi, K. Ado, R. Kanno, Y. Kobayashi, Y. Maki, O. Nakamura and J. B. Goodenough, *J. Solid State Chem.*, 1996, **123**, 255–266.
65 J. M. Tarascon, E. Wang, F. K. Shokoohi, W. R. McKinnon and S. Colson, *J. Electrochem. Soc.*, 1991, **138**, 2859–2864.
66 J. M. Tarascon and D. Guyomard, *J. Electrochem. Soc.*, 1991, **138**, 2864–2868.
67 M. M. Thackeray and R. J. Gummow, *US Pat.*, 5316877, 1994.
68 R. J. Gummow, A. de Kock and M. M. Thackeray, *Solid State Ionics*, 1994, **69**, 59–67.
69 Y. S. Lee, N. Kumada and M. Yoshio, *J. Power Sources*, 2001, **96**, 376–384.
70 R. Benedek and M. M. Thackeray, *Electrochem. Solid-State Lett.*, 2006, **9**, A265–A267.
71 C. Zhan, J. Lu, A. J. Kropf, T. P. Wu, A. N. Jansen, Y. K. Sun, X. P. Qiu and K. Amine, *Nat. Commun.*, 2013, **4**, 2437.
72 T. F. Yi, Y. R. Zhu, X. D. Zhu, J. Shu, C. B. Yue and A. N. Zhou, *Ionics*, 2009, **15**, 779–784.
73 J.-S. Kim, C. S. Johnson, J. T. Vaughey, S. A. Hackney, K. A. Walz, W. A. Zeltner, M. A. Anderson and M. M. Thackeray, *J. Electrochem. Soc.*, 2004, **151**, A1755–A1761.
74 S. W. Lee, K. S. Kim, H. S. Moon, H. J. Kim, B. W. Cho, W. I. Cho, J. B. Ju and J. W. Park, *J. Power Sources*, 2004, **126**, 150–155.
75 S. Lee, M. Jeong and J. Cho, *Adv. Energy Mater.*, 2013, **3**, 1623–1629.
76 L. Jaber-Ansari, K. P. Puntambekar, S. Kim, M. Aykol, L. L. Luo, J. S. Wu, B. D. Myers, H. Iddir, J. T. Russell, S. J. Saldana, R. Kumar, M. M. Thackeray, L. A. Curtiss, V. P. Dravid, C. Wolverton and M. C. Hersam, *Adv. Energy Mater.*, 2015, **5**, 1500646.
77 K. S. Chen, R. Xu, N. S. Luu, E. B. Secor, K. Hamamoto, Q. Q. Li, S. Kim, V. K. Sangwan, I. Balla, L. M. Guiney, J. W. T. Seo, X. K. Yu, W. W. Liu, J. S. Wu, C. Wolverton, V. P. Dravid, S. A. Barnett, J. Lu, K. Amine and M. C. Hersam, *Nano Lett.*, 2017, **17**, 2539–2546.
78 S. B. Chikkannanavar, D. M. Bernardi and L. Y. Liu, *J. Power Sources*, 2014, **248**, 91–100.
79 K. Amine, H. Tukamoto, H. Yasuda and Y. Fujita, *J. Electrochem. Soc.*, 1996, **143**, 1607–1613.
80 E.-S. Lee, K.-W. Nam, E. Hu and A. Manthiram, *Chem. Mater.*, 2012, **24**, 3610–3620.
81 A. D. Robertson and P. G. Bruce, *Chem. Mater.*, 2003, **15**, 1984–1992.
82 L. A. de Picciotto, K. T. Adendorff, D. C. Liles and M. M. Thackeray, *Solid State Ionics*, 1993, **62**, 297–307.
83 G. Pistoia, S. Panero, M. Tocci, R. V. Moshtev and V. Manev, *Solid State Ionics*, 1984, **13**, 311–318.
84 R. Benedek, M. M. Thackeray and L. H. Yang, *J. Power Sources*, 1999, **81**, 487–490.
85 P. Hovington, M. Lagace, A. Guerfi, P. Bouchard, A. Manger, C. M. Julien, M. Armand and K. Zaghib, *Nano Lett.*, 2015, **15**, 2671–2678.
86 M. M. Thackeray, C. S. Johnson, J. T. Vaughey, N. Li and S. A. Hackney, *J. Mater. Chem.*, 2005, **15**, 2257–2267.
87 M. M. Thackeray, S. H. Kang, C. S. Johnson, J. T. Vaughey, R. Benedek and S. A. Hackney, *J. Mater. Chem.*, 2007, **17**, 3112–3125.
88 M. M. Thackeray and M. H. Rossouw, *US Pat.*, 5153081, 1992.
89 M. H. Rossouw, D. C. Liles and M. M. Thackeray, *J. Solid State Chem.*, 1993, **104**, 464–466.
90 Y. Paik, C. P. Grey, C. S. Johnson, J. S. Kim and M. M. Thackeray, *Chem. Mater.*, 2002, **14**, 5109–5115.
91 W. Tang, H. Kanoh, X. Yang and K. Ooi, *Chem. Mater.*, 2000, **12**, 3271–3279.
92 M. H. Rossouw and M. M. Thackeray, *Mater. Res. Bull.*, 1991, **26**, 463–473.
93 C. S. Johnson, S. D. Korte, J. T. Vaughey, M. M. Thackeray, T. E. Bofinger, Y. Shao-Horn and S. A. Hackney, *J. Power Sources*, 1999, **81**, 491–495.
94 P. Kalyani, S. Chitra, T. Mohan and S. Gopukumar, *J. Power Sources*, 1999, **80**, 103–106.
95 A. R. Armstrong, A. D. Robertson and P. G. Bruce, *J. Power Sources*, 2005, **146**, 275–280.
96 F. Capitaine, P. Gravereau and C. Delmas, *Solid State Ionics*, 1996, **89**, 197–202.
97 P. G. Bruce, A. R. Armstrong and R. L. Gitzendanner, *J. Mater. Chem.*, 1999, **9**, 193–198.
98 J. Reed, G. Ceder and A. Van der Ven, *Electrochem. Solid-State Lett.*, 2001, **4**, A78–A81.

99 C. Delmas, I. Saadoune and A. Rougier, *J. Power Sources*, 1993, **44**, 595–602.
100 C. Delmas, M. Menetrier, L. Croguennec, I. Saadoune, A. Rougier, C. Pouillerie, G. Prado, M. Grune and L. Fournes, *Electrochim. Acta*, 1999, **45**, 243–253.
101 E. Rossen, C. D. W. Jones and J. R. Dahn, *Solid State Ionics*, 1992, **57**, 311–318.
102 M. E. Spahr, P. Novak, B. Schnyder, O. Haas and R. Nesper, *J. Electrochem. Soc.*, 1998, **145**, 1113–1121.
103 A. R. Armstrong, A. D. Robertson and P. G. Bruce, *Electrochim. Acta*, 1999, **45**, 285–294.
104 A. D. Robertson, A. R. Armstrong and P. G. Bruce, *Chem. Mater.*, 2001, **13**, 2380–2386.
105 C. Storey, I. Kargina, Y. Grincourt, I. J. Davidson, Y. C. Yoo and D. Y. Seung, *J. Power Sources*, 2001, **97–8**, 541–544.
106 B. Ammundsen, J. Paulsen, I. Davidson, R. S. Liu, C. H. Shen, J. M. Chen, L. Y. Jang and J. F. Lee, *J. Electrochem. Soc.*, 2002, **149**, A431–A436.
107 J. B. Goodenough, A. K. Padhi, K. S. Nanjundaswamy and C. Masquelier, *US Pat.*, 5910382, 1999.
108 A. K. Padhi, K. S. Nanjundaswamy and J. B. Goodenough, *J. Electrochem. Soc.*, 1997, **144**, 1188–1194.
109 A. K. Padhi, K. S. Nanjundaswamy, C. Masquelier, S. Okada and J. B. Goodenough, *J. Electrochem. Soc.*, 1997, **144**, 1609–1613.
110 L. A. de Picciotto and M. M. Thackeray, *Solid State Ionics*, 1986, **18–9**, 773–777.
111 G. G. Amatucci, J. M. Tarascon and L. C. Klein, *J. Electrochem. Soc.*, 1996, **143**, 1114–1123.
112 J. N. Reimers and J. R. Dahn, *J. Electrochem. Soc.*, 1992, **139**, 2091–2097.
113 M. M. Thackeray, C. S. Johnson, K. Amine and J. Kim, *US Pat.*, 6677082, 2004.
114 M. M. Thackeray, C. S. Johnson, K. Amine and J. Kim, *US Pat.*, 6680143, 2004.
115 J. S. Kim, C. S. Johnson and M. M. Thackeray, *Electrochem. Commun.*, 2002, **4**, 205–209.
116 J.-S. Kim, C. S. Johnson, J. T. Vaughey, M. M. Thackeray, S. A. Hackney, W. Yoon and C. P. Grey, *Chem. Mater.*, 2004, **16**, 1996–2006.
117 M. M. Thackeray, S. H. Kang, C. S. Johnson, J. T. Vaughey and S. A. Hackney, *Electrochem. Commun.*, 2006, **8**, 1531–1538.
118 J. R. Croy, M. Balasubramanian, K. G. Gallagher and A. K. Burrell, *Acc. Chem. Res.*, 2015, **48**, 2813–2821.
119 J. Wang, X. He, E. Paillard, N. Laszczynski, J. Li and S. Passerini, *Adv. Energy Mater.*, 2016, **6**, 1600906.
120 J. M. Zheng, S. J. Myeong, W. R. Cho, P. F. Yan, J. Xiao, C. M. Wang, J. Cho and J. G. Zhang, *Adv. Energy Mater.*, 2017, **7**, 1601284.
121 W. D. Li, B. H. Song and A. Manthiram, *Chem. Soc. Rev.*, 2017, **46**, 3006–3059.
122 H. Iddir and R. Benedek, *Chem. Mater.*, 2014, **26**, 2407–2413.
123 H. Iddir, J. Bareño and R. Benedek, *J. Electrochem. Soc.*, 2016, **163**, A1784–A1789.
124 R. Benedek and H. Iddir, *J. Phys. Chem. C*, 2017, **121**, 6492–6499.
125 E. Lee and K. A. Persson, *Adv. Energy Mater.*, 2014, **4**, 1400498.
126 Y. Shin, H. Ding and K. A. Persson, *Chem. Mater.*, 2016, **28**, 2081–2088.
127 S. Kim, M. Aykol, V. I. Hegde, Z. Lu, S. Kirklin, J. R. Croy, M. M. Thackeray and C. Wolverton, *Energy Environ. Sci.*, 2017, **10**, 2201–2211.
128 C. S. Johnson, N. Li, J. T. Vaughey, S. A. Hackney and M. M. Thackeray, *Electrochem. Commun.*, 2005, **7**, 528–536.
129 S. H. Park, S. H. Kang, C. S. Johnson, K. Amine and M. M. Thackeray, *Electrochem. Commun.*, 2007, **9**, 262–268.
130 B. R. Long, J. R. Croy, J. S. Park, J. G. Wen, D. J. Miller and M. M. Thackeray, *J. Electrochem. Soc.*, 2014, **161**, A2160–A2167.
131 K. A. Jarvis, Z. Deng, L. F. Allard, A. Manthiram and P. J. Ferreira, *Chem. Mater.*, 2011, **23**, 3614–3621.
132 J. Reed and G. Ceder, *Electrochem. Solid-State Lett.*, 2002, **5**, A145–A148.
133 Y. Gao, K. Myrtle, M. J. Zhang, J. N. Reimers and J. R. Dahn, *Phys. Rev. B*, 1996, **54**, 16670–16675.
134 B. R. Long, J. R. Croy, F. Dogan, M. R. Suchomel, B. Key, J. Wen, D. J. Miller, M. M. Thackeray and M. Balasubramanian, *Chem. Mater.*, 2014, **26**, 3565–3572.
135 J. Bareño, M. Balasubramanian, S. H. Kang, J. G. Wen, C. H. Lei, S. V. Pol, I. Petrov and D. P. Abraham, *Chem. Mater.*, 2011, **23**, 2039–2050.
136 J. Choi and A. Manthiram, *J. Electrochem. Soc.*, 2005, **152**, A1714–A1718.
137 K. Shizuka, T. Kobayashi, K. Okahara, K. Okamoto, S. Kanzaki and R. Kanno, *J. Power Sources*, 2005, **146**, 589–593.
138 S. H. Park, S. H. Kang, I. Belharouak, Y. K. Sun and K. Amine, *J. Power Sources*, 2008, **177**, 177–183.
139 Z. H. Lu, L. Y. Beaulieu, R. A. Donaberger, C. L. Thomas and J. R. Dahn, *J. Electrochem. Soc.*, 2002, **149**, A778–A791.
140 Z. H. Lu and J. R. Dahn, *J. Electrochem. Soc.*, 2002, **149**, A815–A822.
141 C. S. Johnson, J. S. Kim, C. Lefief, N. Li, J. T. Vaughey and M. M. Thackeray, *Electrochem. Commun.*, 2004, **6**, 1085–1091.
142 A. R. Armstrong, M. Holzapfel, P. Novak, C. S. Johnson, S. H. Kang, M. M. Thackeray and P. G. Bruce, *J. Am. Chem. Soc.*, 2006, **128**, 8694–8698.
143 E. McCalla, A. M. Abakumov, M. Saubanère, D. Foix, E. J. Berg, G. Rousse, M.-L. Doublet, D. Gonbeau, P. Novák, G. Van Tendeloo, R. Dominko and J.-M. Tarascon, *Science*, 2015, **350**, 1516–1521.
144 A. Grimaud, W. T. Hong, Y. Shao-Horn and J. M. Tarascon, *Nat. Mater.*, 2016, **15**, 121–126.
145 D. H. Seo, J. Lee, A. Urban, R. Malik, S. Kang and G. Ceder, *Nat. Chem.*, 2016, **8**, 692–697.
146 C. S. Johnson, N. Li, C. Lefief and M. M. Thackeray, *Electrochem. Commun.*, 2007, **9**, 787–795.
147 S. Muhammad, H. Kim, Y. Kim, D. Kim, J. H. Song, J. Yoon, J.-H. Park, S.-J. Ahn, S.-H. Kang, M. M. Thackeray and W.-S. Yoon, *Nano Energy*, 2016, **21**, 172–184.

148 P. K. Nayak, J. Grinblat, M. Levi, E. Levi, S. Kim, J. W. Choi and D. Aurbach, *Adv. Energy Mater.*, 2016, **6**, 1502398.
149 P. K. Nayak, J. Grinblat, E. Levi, T. R. Penki, M. Levi, Y.-K. Sun, B. Markovsky and D. Aurbach, *ACS Appl. Mater. Interfaces*, 2017, **9**, 4309–4319.
150 J. R. Croy, J. S. Park, Y. Shin, B. T. Yonemoto, M. Balasubramanian, B. R. Long, Y. Ren and M. M. Thackeray, *J. Power Sources*, 2016, **334**, 213–220.
151 M. M. Thackeray, C. Wolverton and E. D. Isaacs, *Energy Environ. Sci.*, 2012, **5**, 7854–7863.
152 K. G. Gallagher, J. R. Croy, M. Balasubramanian, M. Bettge, D. P. Abraham, A. K. Burrell and M. M. Thackeray, *Electrochem. Commun.*, 2013, **33**, 96–98.
153 J. R. Croy, K. G. Gallagher, M. Balasubramanian, Z. Chen, Y. Ren, D. Kim, S.-H. Kang, D. W. Dees and M. M. Thackeray, *J. Phys. Chem. C*, 2013, **117**, 6525–6536.
154 W. I. F. David, unpublished work.
155 G.-A. Nazri and G. Pistoia, *Lithium Batteries: Science and Technology*, Kluwer Academic Publishers, Massachusetts, 2003.
156 N. Leifer, F. Schipper, E. M. Erickson, C. Ghanty, M. Talianker, J. Grinblat, C. M. Julien, B. Markovsky and D. Aurbach, *J. Phys. Chem. C*, 2017, **121**, 9120–9130.
157 M. H. Rossouw, A. Dekock, L. A. Depicciotto and M. M. Thackeray, *Mater. Res. Bull.*, 1990, **25**, 173–182.
158 C. S. Johnson, S. H. Kang, J. T. Vaughey, S. V. Pol, M. Balasubramanian and M. M. Thackeray, *Chem. Mater.*, 2010, **22**, 1263–1270.
159 E. Lee, J. S. Park, H. Kim, Q. Li, J. Wu, V. P. Dravid, J. Blauwkamp, J. Croy and M. M. Thackeray, *DOE Vehicle Technologies Annual Merit Review*, ES049, 2017.
160 D. Kim, G. Sandi, J. R. Croy, K. G. Gallagher, S. H. Kang, E. Lee, M. D. Slater, C. S. Johnson and M. M. Thackeray, *J. Electrochem. Soc.*, 2013, **160**, A31–A38.
161 E. Lee, D. Ahn, J. S. Park, A. Gutierrez, M. He, D. Mohanty, A. Huq, Y. Ren, J. R. Croy and M. M. Thackeray, *DOE Vehicle Technologies Annual Merit Review*, BAT235 & BAT049, 2018.
162 E. Peled and S. Menkin, *J. Electrochem. Soc.*, 2017, **164**, A1703–A1719.
163 C. Li, H. P. Zhang, L. J. Fu, H. Liu, Y. P. Wu, E. Rahm, R. Holze and H. Q. Wu, *Electrochim. Acta*, 2006, **51**, 3872–3883.
164 J. Liu and A. Manthiram, *J. Mater. Chem.*, 2010, **20**, 3961–3967.
165 Y.-K. Sun, M.-J. Lee, C. S. Yoon, J. Hassoun, K. Amine and B. Scrosati, *Adv. Mater.*, 2012, **24**, 1192–1196.
166 H. M. Wu, I. Belharouak, A. Abouimrane, Y. K. Sun and K. Amine, *J. Power Sources*, 2010, **195**, 2909–2913.
167 M. M. Thackeray, C. S. Johnson, J. S. Kim, K. C. Lauzze, J. T. Vaughey, N. Dietz, D. Abraham, S. A. Hackney, W. Zeltner and M. A. Anderson, *Electrochem. Commun.*, 2003, **5**, 752–758.
168 J. Cho, T.-J. Kim, J. Kim, M. Noh and B. Park, *J. Electrochem. Soc.*, 2004, **151**, A1899–A1904.
169 Q. Y. Wang, J. Liu, A. V. Murugan and A. Manthiram, *J. Mater. Chem.*, 2009, **19**, 4965–4972.
170 S. H. Kang and M. M. Thackeray, *Electrochem. Commun.*, 2009, **11**, 748–751.
171 Visual Capitalist, http://www.visualcapitalist.com/nickel-secret-driver-battery-revolution, accessed January 2018.
172 Y.-K. Sun, Z. Chen, H.-J. Noh, D.-J. Lee, H.-G. Jung, Y. Ren, S. Wang, C. S. Yoon, S.-T. Myung and K. Amine, *Nat. Mater.*, 2012, **11**, 942–947.
173 J. R. Croy, A. Gutierrez, E. Lee and M. M. Thackeray, Manganese-Rich Alternatives to Nickel-Rich NMC Cathodes, in preparation.
174 E. Lee, J. Blauwkamp, F. C. Castro, J. Wu, V. P. Dravid, P. Yan, C. Wang, S. Kim, C. Wolverton, R. Benedek, F. Dogan, J. S. Park, J. R. Croy and M. M. Thackeray, *ACS Appl. Mater. Interfaces*, 2016, **8**, 27720–27729.
175 J. Reed and G. Ceder, *Chem. Rev.*, 2004, **104**, 4513–4533.
176 R. J. Gummow, M. M. Thackeray, W. I. F. David and S. Hull, *Mater. Res. Bull.*, 1992, **27**, 327–337.
177 R. J. Gummow, D. C. Liles, M. M. Thackeray and W. I. F. David, *Mater. Res. Bull.*, 1993, **28**, 1177–1184.
178 E. Lee, J. Blauwkamp, A. Gutierrez, M. He, J. Croy and M. M. Thackeray, Stabilizing Low Temperature $LiCoO_2$ by Li_2MnO_3 and Ni Integration, in preparation.
179 M. Sathiya, K. Ramesha, G. Rousse, D. Foix, D. Gonbeau, A. S. Prakash, M. L. Doublet, K. Hemalatha and J. M. Tarascon, *Chem. Mater.*, 2013, **25**, 1121–1131.
180 M. Sathiya, G. Rousse, K. Ramesha, C. P. Laisa, H. Vezin, M. T. Sougrati, M. L. Doublet, D. Foix, D. Gonbeau, W. Walker, A. S. Prakash, M. Ben Hassine, L. Dupont and J. M. Tarascon, *Nat. Mater.*, 2013, **12**, 827–835.
181 P. E. Pearce, A. J. Perez, G. Rousse, M. Saubanere, D. Batuk, D. Foix, E. McCalla, A. M. Abakumov, G. Van Tendeloo, M. L. Doublet and J. M. Tarascon, *Nat. Mater.*, 2017, **16**, 580–586.
182 C. S. Johnson, S. H. Kang, J. T. Vaughey, S. V. Pol, M. Balasubramanian and M. M. Thackeray, *Chem. Mater.*, 2010, **22**, 1263–1270.
183 C. Zhan, Z. Yao, J. Lu, L. Ma, V. A. Maroni, L. Li, E. Lee, E. E. Alp, T. Wu, J. Wen, Y. Ren, C. Johnson, M. M. Thackeray, M. K. Y. Chan, C. Wolverton and K. Amine, *Nat. Energy*, 2017, **2**, 963–971.
184 K. Luo, M. R. Roberts, N. Guerrini, N. Tapia-Ruiz, R. Hao, F. Massel, D. M. Pickup, S. Ramos, Y.-S. Liu, J. Guo, A. V. Chadwick, L. C. Duda and P. G. Bruce, *J. Am. Chem. Soc.*, 2016, **138**, 11211–11218.